Exploring the role of the Sun's motion in terrestrial comet impacts

F. Feng⋆ and C.A.L. Bailer-Jones
Max Planck Institute for Astronomy, Königstuhl 17, 69117 Heidelberg

9 June 2014

ABSTRACT

The cratering record on the Earth and Moon shows that our planet has been exposed to high velocity impacts for much or all of its existence. Some of these craters were produced by the impact of long period comets (LPCs). These probably originated in the Oort cloud, and were put into their present orbits through gravitational perturbations arising from the Galactic tide and stellar encounters, both of which are modulated by the solar motion about the Galaxy. Here we construct dynamical models of these mechanisms in order to predict the time-varying impact rate of LPCs and the angular distribution of their perihelia (which is observed to be non-uniform). Comparing the predictions of these dynamical models with other models, we conclude that cometary impacts induced by the solar motion contribute only a small fraction of terrestrial impact craters over the past 250 Myr. Over this time scale the apparent cratering rate is dominated by a secular increase towards the present, which might be the result of the disruption of a large asteroid. Our dynamical models, together with the solar apex motion, predict a non-uniform angular distribution of the perihelia, without needing to invoke the existence of a massive body in the outer Oort cloud. Our results are reasonably robust to changes in the parameters of the Galaxy model, Oort cloud, and stellar encounters.

Key words: Earth — Galaxy: kinematics and dynamics — methods: statistical — solar-terrestrial relations — comets: general — Oort Cloud

1 INTRODUCTION

1.1 Background

Comet or asteroid impacts on the Earth are potentially catastrophic events which could have a fundamental effect on life on Earth. While at least one extinction event and associated crater is well documented – the K-T impact from 65 Myr ago and the Chicxulub crater (Alvarez et al. 1980; Hildebrand et al. 1991) – a clear connection between other craters and extinction events is less well established. Nonetheless, we know of around 200 large impact craters on the Earth, and doubtless the craters of many other impacts have either since eroded or are yet to be discovered.

Many studies in the past have attempted to identify patterns in the temporal distribution of craters and/or mass extinction events. Some claim there to be a periodic component in the data (e.g. Alvarez & Muller 1984; Raup & Sepkoski 1984; Rohde & Muller 2005; Melott & Bambach 2011), although the reliability of these analyses is debated, and other studies have come to other conclusions (e.g. Grieve & Pesonen 1996 Yabushita 1996 Jetsu & Pelt 2000 Bailer-Jones 2009 Bailer-Jones 2011a; Feng & Bailer-Jones 2013).

Of particular interest is whether these impacts are entirely random, or whether there are one or two dominant mechanisms which account for much of their temporal distribution. Such mech-

anisms need not be deterministic: stochastic models show characteristic distributions in their time series or frequency spectra (e.g. (Bailer-Jones 2012)). We are therefore interested in accounting not for the times of individual impacts, but for the impact rate as a function of time.

In doing this we should distinguish between asteroid and comet impacts. Having smaller relative velocities, asteroid impacts are generally less energetic. Asteroids originate from within a few AU of the Sun, so their impact rate is probably not affected much by events external to the solar system. Comets, on the other hand, originate from the Oort cloud (Oort 1950), and so can be affected by the Galactic environment around the Sun.

As the solar system orbits the Galaxy, it experiences gravitational perturbations from the Galactic tide and from encountering with individual passing stars. These perturbations are strong enough to modify the orbits of Oort cloud comets to inject them into the inner solar system (Wickramasinghe & Napier 2008; Gardner et al. 2011). The strength of these perturbations is dependent upon the local stellar density, so the orbital motion of the Sun will modulate these influences and thus the rate of comet injection and impact to some degree (e.g. Brasser, Higuchi & Kaib (2010); Kaib, Roškar & Quinn (2011); Levison et al. (2010)). As the Sun shows a (quasi-)periodic motion perpendicular to the Galactic plane, and assuming that the local stellar density varies in the same way, it has been argued that this could explain a (supposed) periodic signal in the cratering record. Here we will investigate the connection between the solar motion and the large impact craters

⋆ E-mail:ffeng@mpia.de

(i.e. those generated by high energy impacts) more explicitly. We do this by constructing a dynamical model of the Sun's orbit, the gravitational potential, and the resulting perturbation of comet orbits, from which we will make probabilistic predictions of the time variability of the comet impact rate.

The dates of impact craters are not the only relevant observational evidence available. We also know the orbits of numerous long-period comets (LPCs). The orbits of dynamically new LPCs – those which enter into the inner solar system for the first time – record the angular distribution of the cometary flux. This distribution of their perihelia is found to be anisotropic. Some studies interpret this as an imprint of the origination of comets Bogart & Noerdlinger (1982); Khanna & Sharma (1983), while others believe it results from a perturbation of the Oort Cloud. Under this perturbation scenario, it has been shown that the Galactic tide can (only) deplete the pole and equatorial region of the Oort Cloud (Delsemme 1987) in the Galactic frame, and so cannot account for all the observed anisotropy in the LPC perihelia. It has been suggested that the remainder is generated from the perturbation of either a massive body in the Oort Cloud (Matese, Whitman & Whitmire 1999; Matese & Whitmire 2011) or stellar encounters Biermann, Huebner & Lust (1983); Dybczyński (2002).

1.2 Overview

Assuming a common origin of both the large terrestrial impact craters and the LPCs, we will construct dynamical models of the flux and orbits of injected comets as a function of time based on the solar motion around the Galaxy. Our approach differs from previous work in that we (1) simulate the comet flux injected by the Galactic tide and stellar encounters as they are modulated by the solar motion; (2) use an accurate numerical method rather than averaged Hamiltonian (Fouchard 2004) or Impulse Approximation (Oort 1950; Rickman 1976; Rickman et al. 2005) in the simulation of cometary orbits; (3) take into account the influence from the Galactic bar and spiral arms; (4) test the sensitivity of the resulting cometary flux to varying both the initial conditions of the Sun and the parameters of the Galaxy potential, Oort Cloud, and stellar encounters.

We build the dynamical models as follows. Adopting models of the Galactic potential, Oort Cloud and stellar encounters, we integrate the cometary orbits in the framework of the AMUSE software environment, developed for performing various kinds of astrophysical simulations (Portegies Zwart et al. 2013; Pelupessy et al. 2013). The cometary orbits can be integrated with the perturbation from either the Galactic tide, or stellar encounters, or both. All three are investigated. In principle, we can build a three-parameter dynamical model for the variation of the impacting comet flux as a function of time, Galactic latitude, and Galactic longitude. In practice we reduce this three-parameter model to a 1-parameter model of the variation of the comet impact rate over time, and a 2-parameter model of the angular distribution of the perihelia of LPCs. A further simplification is achieved by replacing the full numerical computations of the perturbations by separating proxies for the tide-induced comet flux and for the encounter-induced comet flux. These are shown to be good approximations which accelerate considerably the computations.

We combine the predictions of the comet impact history with a (parameterized) component which accounts for the crater preservation bias (i.e. older craters are less likely to be discovered) and the asteroid impact rate. We then use Bayesian model comparison to compare the predictions of this model over different ranges of the model parameters to the observed cratering data, using the crater data and statistical method presented in Bailer-Jones (2011a).

We obtain the 2-parameter model for the angular distribution of the perihelia of LPCs by integrating the full 3-parameter model over time. Because we no longer need the time resolution, we actually perform a separate set of numerical simulations to build this model. We then compare our results with data on 102 new comets with accurately determined semi-major axes (the "class 1A" comets of Marsden & Williams (2008)).

This paper is organized as follows. We introduce, in section 2, the data on the craters and LPCs. In section 3 we define our models for the Galactic potential, the Oort cloud, and for stellar encounters, and describe the method for the dynamical simulation of the comet orbits. In section 4 we summarize the Bayesian method of model comparison. In section 5 we use the dynamical model to construct the 1-parameter model of the cometary impact history. In Section 6, we compare our dynamical time series models of the impact history with other models, to assess how well the data support each. In section 7 we use the dynamical model again, but this time to predict the distribution of the perihelia of LPCs (the 2-parameter model), which we compare with the data. A test of the sensitivity of these model comparison results to the model parameters is made in section 8. We discuss our results and conclude in section 9.

The main symbols and acronyms used in this article are summarized in Table 1.

2 DATA

2.1 Terrestrial craters

The data of craters we use in this work is from the *Earth Impact Database* (EID) maintained by the Planetary and Space Science Center at the University of New Brunswick. We restrict our analysis to craters with diameter > 5 km and age < 250 Myr in order to reduce the influence of crater erosion (although an erosion effect is included in our time series models). We select the following data sets defined by Bailer-Jones (2011a)

- **basic150** (32 craters) age $\leqslant 150$ Myr, σ_t original
- **ext150** (36 craters) age $\leqslant 150$ Myr, original or assigned
- **full150** (48 craters) ext150 plus craters with $s^{up} \leqslant 150$ Myr
- **basic250** (42 craters) age $\leqslant 250$ Myr, σ_t original
- **ext250** (46 craters) age $\leqslant 250$ Myr, original or assigned
- **full250** (59 craters) ext250 plus craters with $s^{up} \leqslant 250$ Myr

The terms "basic", "ext", and "full" refer to the inclusion of craters with different kinds of age uncertainties. "original σ_t" means that just craters with measured age uncertainties are included. "original or assigned" adds to this craters for which uncertainties have been estimated. The "full" data sets further include craters with just upper age limits (Bailer-Jones 2011a explains how these can be used effectively). As the size of the existing craters is determined by many factors, e.g. the inclination, velocity and size of the impactor, the impact surface, and erosion, we only use the time of occurrence (s_j) of each impact crater and its uncertainty (σ_j). Figure 1 plots the size and age of the 59 craters we use in the model comparison in Section 6.

2.2 Long-period comets

The LPCs we use are the 102 dynamically new comets (i.e. class 1A) identified by Marsden & Williams (2008) and discussed by

Table 1. Glossary of main acronyms and variables

Symbol	Definition
PDF	probability density function
LSR	local standard of rest
HRF	heliocentric rest frame
BP	before present
LPC	long-period comet
s_j	crater age
σ_t	age uncertainty of crater
s^{up}	upper limit of the age of crater
$\vec{r}_{enc}$	impact parameter or perihelion of encounter
$\vec{v}_\star$	velocity of a star in the LSR
$\vec{v}_{enc}$	velocity of the stellar encounter relative to the Sun
$b_\star$	Galactic latitude of $\vec{v}_\star$
$l_\star$	Galactic longitude of $\vec{v}_\star$
b_{enc}	Galactic latitude of $\vec{v}_{enc}$
l_{enc}	Galactic longitude of $\vec{v}_{enc}$
b_p	Galactic latitude of the perihelion of a stellar encounter
l_p	Galactic longitude of the perihelion of a stellar encounter
b_c	Galactic latitude of cometary perihelion
l_c	Galactic longitude of cometary perihelion
q	perihelion distance
a	semi-major axis
e	eccentricity
M_{enc}	mass of a stellar encounter
v_{enc}	speed of a star at encounter
r_{enc}	distance of a star at encounter
f_c	injected comet flux relative to the total number of comets
$\bar{f}_c$	averaged f_c over a time scale
γ	parameter of impact intensity $\frac{M_{enc}}{v_{enc}r_{enc}}$
γ_{bin}	normalized maximum γ in a time bin
G_1, G_2	coefficients of radial tidal force
G_3	coefficient of vertical tidal force
ρ	stellar density
η	ratio between the trend component and f_c
ξ	ratio between the tide-induced flux and encounter-induced flux
κ	angle between $\vec{r}_{enc}$ and the solar apex
M_s	mass of the Sun

Figure 1. The diameters and ages of the 59 craters with (bottom) and without (top) age uncertainties plotted. The blue points/lines indicate the craters with assigned age uncertainties. The red lines/brackets indicate the upper ages of the craters without well-defined ages. Adapted from Bailer-Jones (2011a).
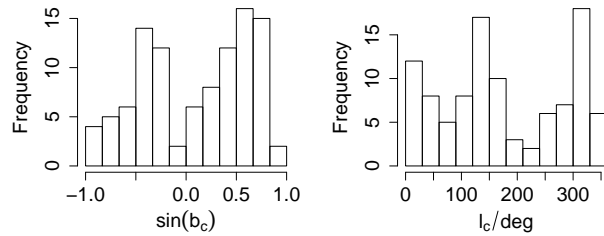
Figure 2. The distribution of $\sin b_c$ (left panel) and l_c (right panel) of perihelia of the 102 LPCs.

Matese & Whitmire (2011). Figure 2 shows the distribution over the Galactic latitude (b_c) and longitude (l_c) of the cometary perihelia. [1] The two peaks in the longitude distribution suggest a great circle on the sky passing through $l = 135°$ and $l = 315°$ (Matese, Whitman & Whitmire 1999; Matese & Whitmire 2011). We explain this anisotropy in Section 7.

3 SIMULATION OF COMETARY ORBITS

We now build dynamical models of the Oort cloud comets and their perturbation via the Galactic tide and stellar encounters by simulating the passage of the solar system through the Galaxy. We first introduce the Galactic potential, which yields a tidal gravitational force on the Sun and Oort Cloud comets. Then we give the initial conditions of the Oort cloud and the distribution of stellar encounters. Then we outline the numerical methods used to calculate the solar motion and the comet orbits.

3.1 Galactic potential

We adopt a Galactic potential with three components, namely an axisymmetric disk and a spherically symmetric halo and bulge

$$\Phi_{sym} = \Phi_b + \Phi_h + \Phi_d \tag{1}$$

(this is same model as in Feng & Bailer-Jones (2013)). The components are defined (in cylindrical coordinates) as

$$\Phi_{b,h} = -\frac{GM_{b,h}}{\sqrt{R^2 + z^2 + b_{b,h}^2}}, \tag{2}$$

$$\Phi_d = -\frac{GM_d}{\sqrt{R^2 + (a_d + \sqrt{(z^2 + b_d^2)})^2}}, \tag{3}$$

where R is the disk-projected galactocentric radius of the Sun and z is its vertical displacement above the midplane of the disk. M is the mass of the component, b and a are scale lengths, and G is

---

[1] Note that our angular distribution is different from the one given in Matese & Whitmire (2011) because the direction of perihelion is opposite to that of aphelion.
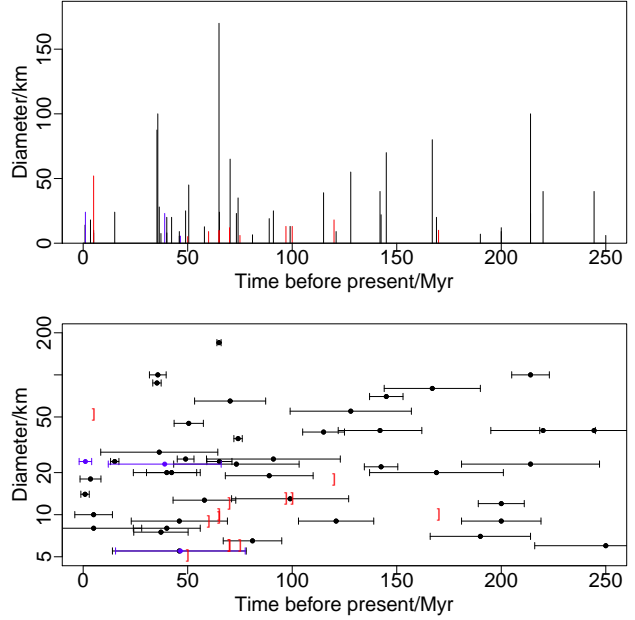
Table 2. The parameters of the Galactic potential model for the symmetric component (García-Sánchez et al. 2001), the arm (Cox & Gómez 2002; Wainscoat et al. 1992), and the bar (Dehnen 2000).

component	parameter value
Bulge	$M_b = 1.3955 \times 10^{10}\ M_\odot$
	$b_b = 0.35\,\mathrm{kpc}$
Halo	$M_h = 6.9766 \times 10^{11}\ M_\odot$
	$b_h = 24.0\,\mathrm{kpc}$
Disk	$M_d = 7.9080 \times 10^{10}\ M_\odot$
	$a_d = 3.55\,\mathrm{kpc}$
	$b_d = 0.25\,\mathrm{kpc}$
Arm	$\zeta = 15°$
	$R_{\min} = 3.48\,\mathrm{kpc}$
	$\phi_{\min} = -20°$
	$\rho_0 = 2.5 \times 10^7 M_\odot \mathrm{kpc}^{-3}$
	$r_0 = 8\,\mathrm{kpc}$
	$R_s = 7\,\mathrm{kpc}$
	$H = 0.18\,\mathrm{kpc}$
	$\Omega_s = 20\,\mathrm{km}s^{-1}/\mathrm{kpc}$
bar	$R_b/R_{\mathrm{CR}} = 0.8$
	$\alpha = 0.01$
	$R_{\mathrm{CR}} = R_\odot(t = 0\,\mathrm{Myr})/2$
	$\alpha = 0.01$
	$\Omega_b = 60\,\mathrm{km}s^{-1}/\mathrm{kpc}$

the gravitational constant. We adopt the values of these parameters from García-Sánchez et al. (2001), which are listed in Table 2.

In Section 8 we will add to this non-axisymmetric and time-varying components due to spiral arms and the Galactic bar, to give the new potential

$$\Phi_{\mathrm{asym}} = \Phi_{\mathrm{sym}} + \Phi_{\mathrm{arm}} + \Phi_{\mathrm{bar}}\,, \tag{4}$$

where Φ_{arm} is a potential of two logarithmic arms from Wainscoat et al. (1992) with parameters given in Feng & Bailer-Jones (2013), and Φ_{bar} is a quadrupole potential of rigid rotating bar from Dehnen (2000). These components are used in the potential for the calculation of the solar orbit, but not the stellar encounter rate discussed in section 3.3.

The geometry of the arm is

$$\phi_s(R) = \log(R/R_{\min})/\tan(\zeta) + \phi_{\min}, \tag{5}$$

where ζ is the pitch angle, $R_{\min}$ is the inner radius, and $\phi_{\min}$ is the azimuth at that inner radius. A default pattern speed of $\Omega_p = 20$ km s^{-1} kpc^{-1} is adopted (Martos et al. 2004; Drimmel 2000). The corresponding potential of this arm model is

$$\Phi_{arm} = -\frac{4\pi G H}{K_1 D_1} \rho_0 e^{-\frac{R-r_0}{R_s}}$$
$$\times \cos(N[\phi - \phi_s(R, t)]) \left[\mathrm{sech}\left(\frac{K_1 z}{\beta_1}\right)\right]^{\beta_1}, \tag{6}$$

where

$$K_1 = \frac{N}{R\sin\zeta},$$
$$\beta_1 = K_1 H(1 + 0.4 K_1 H),$$
$$D_1 = \frac{1 + K_1 H + 0.3(K_1 H)^2}{1 + 0.3 K_1 H},$$

and N is the number of spiral arms. The parameters in equation 6 are given in Table 2.

The bar potential is a 2D quadrupole Dehnen (2000). Because the Sun always lies outside of the bar, we adopt the potential

$$\Phi_{bar} = -A_b \cos[2(\phi - \Omega_b t - \phi_{\min})]\left[\left(\frac{R}{R_b}\right)^3 - 2\right]\quad R \geqslant R_b \tag{7}$$

where R_b and Ω_b are the size and pattern speed of the bar respectively and $\phi_{\min}$ is the bar angle. We assume that the spiral arms start from the ends of the major axis of the bar. We only consider the barred state and ignore the evolution of the bar, so we adopt a constant amplitude for the quadrupole potential, i.e. $A_b = A_f$, in equation (3) of Dehnen (2000). A_f is determined by the definition of the bar strength

$$\alpha \equiv 3\frac{A_f}{v^2}\left(\frac{R_b}{R}\right)^3, \tag{8}$$

where R and v are the current galactocentric distance of the Sun and the corresponding local circular velocity. The fixed bar strength is given in Table 2, from which we calculate A_f and hence A_b.

3.2 Oort Cloud

We generate Oort cloud comets using two different models, one from Duncan, Quinn & Tremaine (1987) (hereafter DQT) with the parameters defined in Rickman et al. (2008), and another which we have reconstructed from the work of Dones et al. (2004a) (hereafter DLDW).

In the DQT model, initial semi-major axes (a_0) for comets are selected randomly from the interval [3000, 10^5] AU with a probability density proportional to $a_0^{-1.5}$. The initial eccentricities (e_0) are selected with a probability density proportional to e_0 (Hills 1981), in such a way that the perihelia (q_0) are guaranteed to be larger than 32 AU. We generate the other orbital elements — $\cos i_0$, ω_0, Ω_0 and M_0 — from uniform distributions. Because the density profile of comets is proportional to $r^{-3.5}$, where r is the sun-comet distance, about 20% of the comets lie in the classical Oort Cloud ($a > 20\,000$ AU).

In the DLDW model, the initial semi-major axes, eccentricities, and inclination angles are generated by Monte Carlo sampling from the relevant distributions shown in Dones et al. (2004a). This produces semi-major axes in the range 3000 to 100 000 AU and ensures that the perihelia are larger than 32 AU. Unlike the DQT model, there is a dependency of the cometary eccentricity and inclination on the semi-major axis, as can be see in Figures 1 and 2 of Dones et al. (2004b). We generate comet positions and velocities relative to the invariant plane and then transform these into vectors relative to the Galactic plane. In doing so we adopted values for the Galactic longitude and latitude of the north pole of the invariant plane of 98° and 29° respectively.

The distributions of the cometary heliocentric distances for the DQT and DLDW models are given in Figure 3. We see that the DQT model produces more comets in the inner Oort cloud ($< 20\,000$ AU) and the DLDW model more in the outer Oort Cloud ($> 20\,000$ AU). Our distributions differ slightly from those in Figure 3 of Dybczyński (2002) because our initial semi-major axes have different boundaries, and because our reconstruction of initial eccentricities and inclination angles is slightly different from the approach used in Dybczyński (2002). Many other Oort cloud initial conditions have been constructed numerically (Emel'yanenko, Asher & Bailey 2007; Kaib, Roškar & Quinn 2011). Given the inherent uncertainty of the Oort cloud's true initial conditions, we carry out our work using two different Oort cloud models and investigate the sensitivity of our results to this (e.g. in section 7).
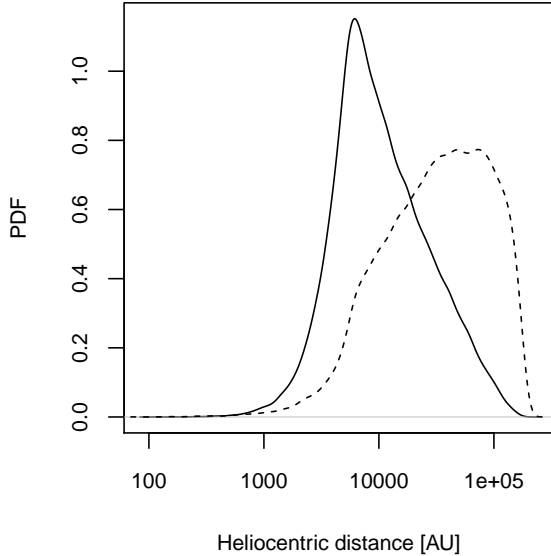
Figure 3. The normalized distributions of initial heliocentric distances of comets generated from the DQT model (solid line) and DLDW model (dashed line) with a sample size of 10^5.
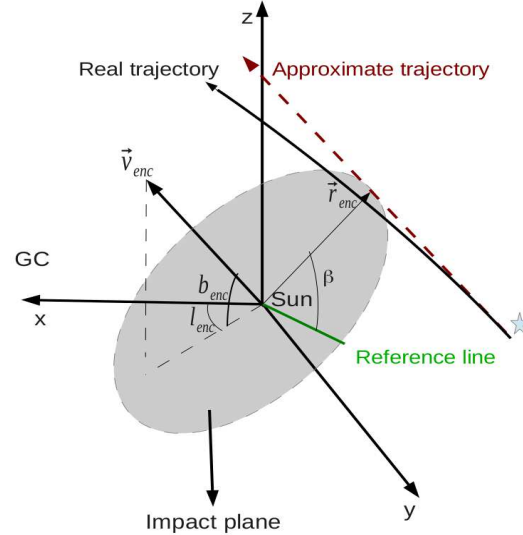

Figure 4. Schematic illustration in the heliocentric rest frame of stellar encounters. The circle is the impact plane which is defined by its normal, the encounter velocity $\vec{v}_{\mathrm{enc}}$. β is the angle in the impact plane measured from the reference axis to the stellar perihelion (i.e. the encounter). The vector in this plane from the Sun to the position of the encounter (i.e. the stars perihelion) is defined as r_{enc}. b_{enc} and l_{enc} are the Galactic latitude and longitude of $\vec{v}_{\mathrm{enc}}$, respectively. (x, y, z) is the Galactic coordinate system. $\vec{r}_{\mathrm{enc}}$ is defined as the shortest distance from the Sun to the approximate trajectory which is a straight line in the direction of $\vec{v}_{\mathrm{enc}}$. The approximate trajectory of an encounter is used for the definition of encounter perihelion $\vec{r}_{\mathrm{enc}}$ while the real trajectory is integrated through simulations.

3.3 Stellar encounters

The geometry of encounters is complicated by the Sun's motion relative to the local standard of rest (LSR). This solar apex motion could, by itself, produce an anisotropic distribution in the directions of stellar encounters in the heliocentric rest frame (HRF). Any anisotropy must be taken into account when trying to explain the observed anisotropic perihelia of the LPCs. Nonetheless, Rickman et al. (2008) simulated cometary orbits with an isotropic distribution of stellar encounters which is inconsistent with their method for initializing encounters. Here we use their method to generate encounters, but now initialize stellar encounters self-consistently to have a non-uniform angular distribution.

3.3.1 Encounter scenario

The parameters of stellar encounters are generated using a Monte Carlo sampling method, as follows. We distribute the encounters into different stellar categories (corresponding to different types of stars) according to their frequency, F_i, as listed in Table 8 of García-Sánchez et al. (2001). In each stellar category, the stellar mass M_i, Maxwellian velocity dispersion $\sigma_{\star i}$, and solar peculiar velocity $v_{\odot i}$, are given. The encounter scenario in the HRF is illustrated in Figure 4. The encounter perihelion $\vec{r}_{\mathrm{enc}}$ direction (which has Galactic coordinates b_p and l_p) is by definition perpendicular to the encounter velocity $\vec{v}_{\mathrm{enc}}$. The angle β is uniformly distributed in the interval of $[0, 2\pi]$.

In this encounter scenario in the HRF, the trajectory of a stellar encounter is determined by the encounter velocity $\vec{v}_{\mathrm{enc}}$, the encounter perihelion $\vec{r}_{\mathrm{enc}}$, and the encounter time t_{enc}. In the following paragraphs, we will first find the probability density function (PDF) of encounters for each stellar category as a function of t_{enc}, r_{enc}, and v_{enc}, and then sample these parameters from this using the Monte Carlo method introduced by Rickman et al. (2008) (hereafter R08). Then we will sample b_{enc} and l_{enc} using a revised

version of R08's method. Finally, b_p and l_p can be easily sampled because $\vec{r}_{\mathrm{enc}}$ is perpendicular to $\vec{v}_{\mathrm{enc}}$.

3.3.2 Encounter probability

The probability for each category of stars is proportional to the number of stars passing through a ring with a width of dr_{enc} and centered on the Sun. The non-normalized PDF is therefore just

$$P_u(t_{\mathrm{enc}}, r_{\mathrm{enc}}, v_{\mathrm{enc}}) = 4\pi n_i v_{\mathrm{enc}} r_{\mathrm{enc}} \propto \rho(t_{\mathrm{enc}}) v_{\mathrm{enc}} r_{\mathrm{enc}}, \qquad (9)$$

where n_i is the local stellar number density of the ith category of stellar encounters, and $\rho(t_{\mathrm{enc}})$ is the local stellar mass density, which will change as the Sun orbits the Galaxy.[2] Thus the encounter probability is proportional to the local mass density, the encounter velocity and the encounter perihelion. We use a Monte Carlo method to sample t_{enc}, v_{enc}, and r_{enc} from this.

In different application cases, we sample the encounter time t_{enc} over different time spans according to equation 9, where the local mass density is calculated using Poisson's equation with the potentials introduced in section 3.1. Although we may simulate stellar encounters over a long time scale, we ignore the change of the solar apex velocity and direction when simulating the time-varying comet flux (in section 5) and the angular distribution of current LPCs (in section 7). We select r_{enc} with a PDF proportional to r_{enc}

---

[2] We assume that the mass densities of different stellar categories have the same spatial distribution.

with an upper limit of 4×10^5 AU. However, the sampling process of v_{enc} is complicated by the solar apex motion and the stellar velocity in LSR, which we accommodate in the following way.

The encounter velocity in the HRF, $\vec{v}_{enc}$, is the difference between the velocity of the stellar encounter in the LSR, $\vec{v}_\star$, and the solar apex velocity relative to that type of star (category i) in the LSR, $\vec{v}_{\odot i}$, i.e.[3]

$$\vec{v}_{enc} = \vec{v}_\star - \vec{v}_{\odot i} \ . \tag{10}$$

We can consider the above formulae as a transformation of a stellar velocity from the LSR to the HRF. The magnitude of this velocity in the HRF is

$$v_{enc} = [v_\star^2 + v_{\odot i}^2 - 2v_{\odot i}v_\star \cos \delta]^{1/2} \ , \tag{11}$$

where δ is the angle between $\vec{v}_\star$ and $\vec{v}_{\odot i}$ in the LSR.

To sample v_{enc}, it is necessary to take into account both the encounter probability given in equation 9 and the distribution of $v_\star$. We generate $v_\star$ using

$$v_\star = \sigma_{\star i} \left[\frac{1}{3}(\eta_u^2 + \eta_v^2 + \eta_w^2) \right]^{1/2} , \tag{12}$$

where $\sigma_{\star i}$ is the stellar velocity dispersion in the ith category, and η_u, η_v, η_w are random variables, each following a Gaussian distribution with zero mean and unit variance.

We then realize the PDF of encounters over v_{enc} (i.e. $P_u \propto v_{enc}$) using R08's method as follows: (i) we randomly generate δ to be uniform in the interval $[0, 2\pi]$; (ii) adopting $v_{\odot i}$ from table 1 in R08 and generating $v_\star$ from equation 12, we calculate v_{enc} using equation 11; (iii) we define a large velocity $V_{enc} = v_{\odot i} + 3\sigma_{\star i}$ for the relevant star category and randomly draw a velocity v_{rand} from a uniform distribution over $[0, V_{enc}]$. If $v_{rand} < v_{enc}$, we accept v_{enc} and the values of the generated variables $\delta, v_\star$. Otherwise, we reject it and repeat the process until $v_{rand} < v_{enc}$.

We generate 10^5 encounters in this way. Figure 5 shows the resulting distribution of v_{enc}. It follows a positively-constrained Gaussian-like distribution with mean velocity of 53 km/s and a dispersion of 21 km/s, which is consistent with the result in R08. In their modelling, R08 adopt a uniform distribution for $\sin b_{enc}$, and l_{enc}. This is not correct, however, because encounters are more common in the direction of the solar antapex where the encounter velocities are larger than those in other directions (equation 9). We will show how to find the true distribution of $\sin b_{enc}$, l_{enc}, $\sin b_p$ and l_p as follows.

3.3.3 Anisotropic perihelia of encounters

To complete the sampling process of encounters, we need to find a 5-variable PDF, i.e. $P_u(t_{enc}, r_{enc}, v_{enc}, b_{enc}, l_{enc})$. We have used R08's original Monte Carlo method to generate t_{enc}, r_{enc} and v_{enc} according to equation 9. However, b_{enc} and l_{enc} are not generated because R08 only use equation 11 to generate the magnitude of $\vec{v}_{enc}$ rather than the direction of $\vec{v}_{enc}$. To sample the directions of $\vec{v}_{enc}$, we change the first and second steps in R08's method introduced in section 3.3.2 as follows: (i) we randomly generate $\{b_\star, l_\star\}$ such that $\sin b_\star$ and $l_\star$ are uniform in the interval of $[-1, 1]$ and $[0, 2\pi]$, respectively; (ii) adopting $b_{apex} = 58.87°$ and $l_{apex} = 17.72°$ for
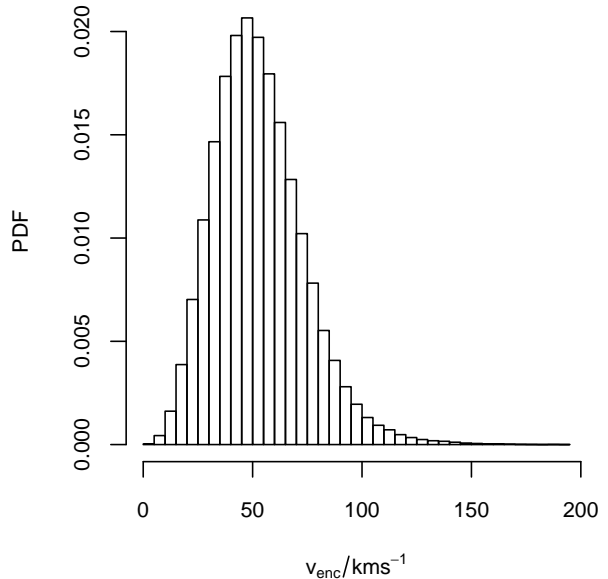

Figure 5. The histogram of the distribution of v_{enc} of all types of stars. The total number of encounters is 197 906, which is the set of simulated encounters over the past 5 Gyr.

the solar apex direction and generating $v_\star$ according to equation 12, we calculate $\vec{v}_{enc}$ according to equation 10.

Selected in this way, $\sin b_\star$, $l_\star$, $\sin b_{enc}$, and l_{enc} all have non-uniform distributions. The Galactic latitude b_p and longitude l_p of the encounter perihelia are also not uniform. Like R08, we draw 197 906 encounters over the past 5 Gyr from our distribution of encounters. The resulting histograms of $\sin b_{enc}$, l_{enc}, $\sin b_p$, and l_p are shown in Figure 6. We see that the encounter velocity, $\vec{v}_{enc}$, concentrates in the antapex direction, while the encounter perihelion, $\vec{r}_{enc}$, concentrates in the plane perpendicular to apex-antapex direction. In addition, the distribution of l_p is flatter than that of l_{enc} because $\vec{r}_{enc}$ concentrates on a plane rather than along a direction.

In order to clarify the effect of the solar apex motion, we define κ as the angle between the encounter perihelion $\vec{r}_{enc}$ and the solar apex. If there were no solar apex motion, $\cos \kappa$ would be uniform. The effect of solar apex motion is shown in Figure 7. The solar apex motion would result in the concentration of encounter perihelia on the plane perpendicular to the apex direction. This phenomenon is detected by García-Sánchez et al. (2001) using Hipparcos data, although the observational incompleteness biases the data. The non-uniform distribution over $\cos \kappa$ results in an anisotropy in the perihelia of LPCs, as we will demonstrate and explain in Section 7.

3.4   Methods of numerically simulating the comet orbits

3.4.1   AMUSE

Taking the above models and initial conditions, we construct an integrator for the orbits of Oort cloud comets via a procedure similar to that in Wisdom & Holman (1991), using the Bridge method (Fujii et al. 2007) in the AMUSE framework[4] (a platform for coupling existing codes from different domains; Pelupessy et al. 2013; Portegies Zwart et al. 2013). A direct integration of the cometary

---

[3] We define a symbol without using the subscript i when the symbol is derived from a combination of symbols belonging and not belonging to certain stellar category.
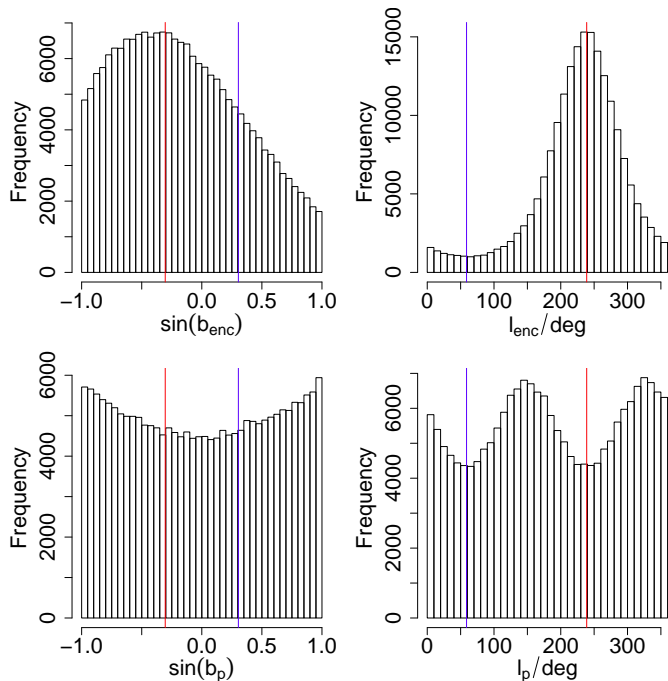
[4] http://www.amusecode.org

Figure 6. The upper panels show the distributions of the directions of the stellar encounter velocities in our simulations in Galactic coordinates as $\sin b_{enc}$ (upper left) and l_{enc} (upper right). The lower panels show the distributions of the directions of the corresponding perihelia as $\sin(b_p)$ (lower left) and l_p (lower right). The blue and red lines denote the apex and antapex directions, respectively. The total number of encounters is 197 906, which is the set of simulated encounters over the past 5 Gyr.
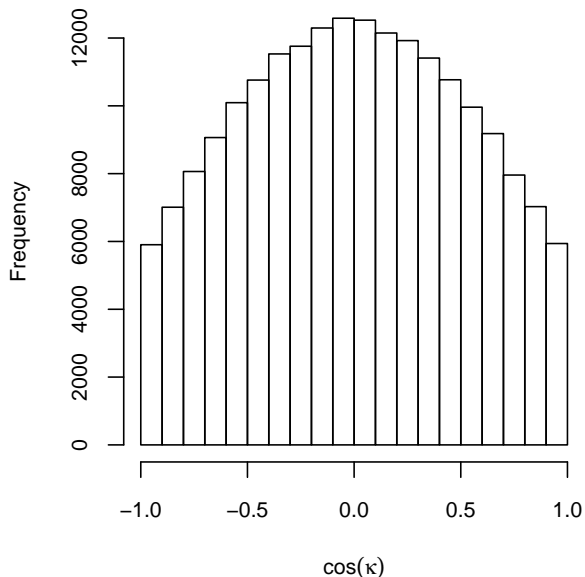

Figure 7. The distribution of the cosine of the angle between the encounter perihelion and the solar apex.

orbits is computationally expensive due to the high eccentricity orbits and the wide range of timescales involved. We therefore split the dynamics of the comets into Keplerian and interaction terms (following Wisdom & Holman 1991). The Keplerian part has an analytic solution for arbitrary time steps, while the interaction terms of the Hamiltonian consist only of impulsive force kicks. To achieve this we split the Hamiltonian for the system in the following way

$$H = H_{\mathrm{Kepler}} + H_{\mathrm{encounter}} + H_{\mathrm{tide}} \qquad (13)$$

where H_{Kepler}, $H_{\mathrm{encounter}}$, and H_{tide} describe the interaction of the comet with the dominant central object (the Sun), a passing star, and the Galactic tide, respectively. Specifically, the Keplerian cometary orbits can be integrated analytically according to H_{Kepler} while the interactions with the Galactic tide and stellar encounters are taken into account in terms of force kicks. For the time integration a second order leapfrog scheme is used, where the Keplerian evolution is interleaved with the evolution under the interaction terms. The forces for the latter are calculated using direct summation, in which the comet masses are neglected. Meanwhile, the Sun moves around the Galactic center under the forces from the Galactic tide and stellar encounters calculated from $H_{\mathrm{encounter}}$ and H_{tide} in the leapfrog scheme.

We first initialize the orbital elements of the Sun and encountering stars about the Galaxy, and the Oort cloud comets about the Sun. We treat the stellar encounters as a N-body system with a varying number of particles, simulated using the Huayno code Pelupessy, Jänes & Portegies Zwart 2012. The interaction between comets and the Sun is simulated with a Keplerian code based on Bate, Mueller & White (1971).

At each time step in the orbital integration we calculate the gravitational force from the Galaxy and stellar encounters. The velocities of the comets are changed according to the Hamiltonian in equation 13 at every half time step. Meanwhile, each comet moves in its Keplerian orbit at each time step. All variables are transformed into the HRF in order to take into account the influence of the solar motion and stellar encounters on the cometary orbits.

We use constant time steps in order to preserve the symplectic properties of the integration scheme in AMUSE (although we note that a symplectically corrected adaptive time step is used in some codes, such as SCATR (Kaib, Quinn & Brasser 2011)). We use a time step of 0.1 Myr for tide-only simulations because we find no difference in the injected flux when simulated using a smaller time step. The choice of time step size is a trade-off between computational speed and sample noise in the injected comet sample. We use a time step of 0.01 Myr in the encounter-only and in the combined (tide plus encounter) simulations when modelling the angular distribution of the LPCs' perihelia (section 7). (In section 8 we repeat some of these simulations with a shorter time step – 0.001 Myr – to confirm that this time step is small enough.) We use a time step of 0.001 Myr in all other simulations.

In the following simulations we adopt the initial velocity of the Sun from Schönrich, Binney & Dehnen (2010) and the initial galactocentric radius from Schönrich (2012). Other initial conditions and their uncertainties are the same as in Feng & Bailer-Jones (2013). The circular velocity of the Sun (at $R = 8.27\,\mathrm{kpc}$), $v = 225.06$ km/s, is calculated based on the axisymmetric Galactic model in Section 3.1. These values are listed in Table 3.

Table 3. The current phase space coordinates of the Sun, represented as Gaussian distributions, and used as the initial conditions in our orbital model (Schönrich, Binney & Dehnen 2010; Schönrich 2012; Majaess, Turner & Lane 2009; Dehnen & Binney 1998).

	R/kpc	V_R/kpc Myr^{-1}	ϕ/rad	$\dot{\phi}$/rad Myr^{-1}	z/kpc	V_z /kpc Myr^{-1}
mean	8.27	-0.01135	0	0.029	0.026	-0.0074
standard deviation	0.5	0.00036	0	0.003	0.003	0.00038

3.4.2 Numerical accuracy of the AMUSE-based method

To test the numerical accuracy of the AMUSE-based method, we generated 1000 comets from the DLDW model and monitored the conservation of orbital energy and angular momentum. As the perturbation from the Galactic potential and stellar encounters used in our work would violate conservation of the third component of angular momentum (L_z), we use a simplified Galactic potential for this test, namely a massive and infinite sheet with

$$\Phi_{\text{sheet}} = 2\pi G\sigma|z|, \tag{14}$$

where G is the gravitational constant, $\sigma = 5.0 \times 10^6 \ M_\odot/\text{kpc}^2$ is the surface density of the massive sheet and z is the vertical displacement from the sheet. Because this potential imposes no tidal force on comets if the Sun does not cross the disk, it enables us to test the accuracy of the bridge method in AMUSE by using the conservation of cometary orbital energy and the angular momentum perpendicular to the sheet. To guarantee that the Sun does not cross the plane during the 1 Gyr orbital integration (i.e. the oscillation period is more than 2 Gyr), we adopt the following initial conditions of the Sun: $R = 0$ kpc, $\phi = 0$, $z = 0.001$ kpc, $V_R = 0$ kpc/Myr, $\dot{\phi} = 0$ rad/Myr, $V_z = 0.0715$ kpc/Myr. Integrating the cometary orbits over 1 Gyr with a constant time step of 0.1 Myr, we calculate the fractional change of the comets' orbital energies E and the vertical component of their angular momenta L_z during the motion (Figure 8). Both quantities are conserved to a high tolerance, with fractional changes of less than 10^{-6} for L_z and less than 10^{-12} for E. The numerical errors are independent of the comet's energy (which is inversely proportional to the semi-major axis). Compared to the magnitude of the perturbations which inject comets from the Oort cloud into the observable zone, these numerical errors can be ignored during a 1 Gyr and even a 5 Gyr integration.

3.4.3 Comparison of the AMUSE-based method with other methods

Our numerical method calculates perturbations from stellar encounters and the Galactic tide using dynamical equations directly, instead of employing an impulse approximation (e.g. CIA, DIA, or SIA Rickman et al. (2005)) or the Averaged Hamiltonian Method (AHM)(Fouchard 2004). In the latter the Hamiltonian of the cometary motion is averaged over one orbital period. This can significantly reduce the calculation time, but is potentially less accurate. A more explicit method is to integrate the Newtonian equations of motion directly, e.g. via the Cartesian Method (CM) of (Fouchard 2004), but this is more time consuming.

To illustrate the accuracy of the AHM, CM, and AMUSE-based methods in simulating high eccentricity orbits, we integrate the orbit of one comet using all methods. The test comet has a semi-major axis of $a = 25\,000$ AU and an eccentricity of $e = 0.996$ (as used in Fouchard (2004)). Adopting the following initial conditions of the Sun – $R = 8.0$ kpc, $\phi = 0$, $z = 0.026$ kpc, $V_R = -0.01$ kpc/Myr, $\dot{\phi} = 0.0275$ rad/Myr, $V_z = 0.00717$ kpc/Myr –
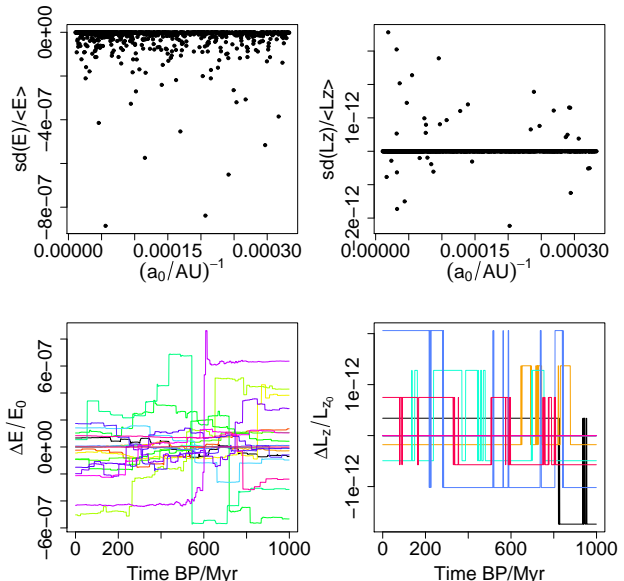

Figure 8. Assessment of the numerical accuracy of the AMUSE-based method through monitoring the conservation of energy E and angular momentum L_z for 1000 comets generated from the DLDW Oort cloud model. Upper panels: For each of the 1000 comets, the standard deviation (over its orbit) of E (left) and L_z (right) relative to the average value over the orbit, plotted as a function of the initial energy (which is proportional to $1/a_0$). Lower panels: the fractional change over the orbit of E and L_z for the 20 comets (represented by different colours) with the highest numerical errors.

and using the same tide model as described above, the solar orbit under the perturbation from the Galactic tide is integrated over the past 5 Gyr. Figure 9 shows that the evolutions of the cometary perihelia calculated using the CM and AMUSE-based methods are very similar, whereas AHM shows an evolution which diverges from these. As CM is the most accurate method, this shows that the AHM cannot be used to accurately calculate the time-varying, because it holds the perturbing forces constant during each orbit. Because the AMUSE-based method computes a large sample of comets more efficiently than CM does, we have adopted the AMUSE-based method in our work.

3.4.4 Calculation of the injected comet flux

A comet which comes too close to the perturbing effects of the giant planets in the solar system will generally have its orbit altered such that it is injected into a much shorter periodic orbit or is ejected from the solar system on an unbound orbit. We regard a comet as having been injected into the inner solar system in this way when it enters into the "loss cone" (Wiegert & Tremaine 1999), i.e. that region with a heliocentric radius of 15 AU or less (the same definition as in Dybczyński (2005) and R08). These are the comets which can then, following further perturbations from the planets, hit the
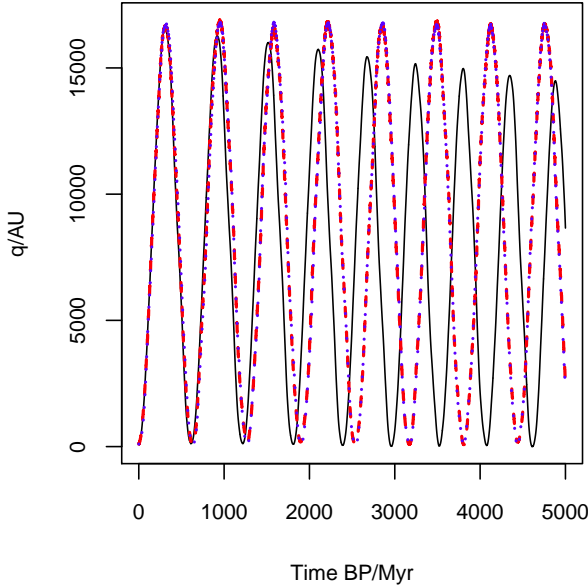
Figure 9. The variation of the perihelion of one comet calculated with three different integration methods: AHM (black solid), CM (red dashed), and AMUSE-based method (blue dotted).

Earth. If injected comets enter an observable zone within $< 5\,\mathrm{AU}$ then they may be observed as a LPC. Comets which are injected into the loss cone or which are ejected from the solar system (i.e. achieve heliocentric distances larger than $4 \times 10^5\,\mathrm{AU}$) are removed from the simulation.

The observable comets are only a subset of the injected comets because some injected comets can be ejected again by Saturn and Jupiter. But assuming that this is independent of the orbital elements over long time scales, we assume that the flux of injected comets is proportional to the flux of LPCs. Inner Oort cloud comets, in particular comets with $a < 3000\,\mathrm{AU}$, may be injected into the loss cone ($q < 15\,\mathrm{AU}$) but not enter the observable zone ($q < 5\,\mathrm{AU}$) (Kaib & Quinn 2009). In our simulations we will examine the properties of comets injected into both types of target zone, and we will refer to such injected comets as LPCs. Once we have identified the injected comets, we calculate the Galactic latitudes b_c and longitudes l_c of their perihelia. Because the orbital elements of the class 1A LPCs are recorded during their first passage into inner solar system, we can reasonably assume that the direction of the LPC perihelion is unchanged after entering the "loss cone". In Section 5 and 7, we will model the terrestrial cratering time series and the anisotropic perihelion of LPCs based on the injected comet flux. Specifically, in Section 5, we will show how we convert the simulations of the perturbations of the cometary orbits into a model for the time variation of the cometary flux entering the inner solar system.

4 BAYESIAN INFERENCE METHOD

We summarize here our Bayesian method for quantifying how well a time series model can describe a set of cratering data (or indeed any other series of discrete time measurements with uncertainties). A full description of the method and its application to the cratering data for various non-dynamical models can be found in Bailer-Jones (2011a,b).

4.1 Evidence

If we define D as the time series of craters and M as some model for these data, then the evidence of the model is defined as

$$P(D|M) = \int_\theta P(D|\theta, M)P(\theta|M)d\theta, \qquad (15)$$

where θ is the parameters of the model, and $P(D|\theta, M)$ and $P(\theta|M)$ are the likelihood of the data and the prior distribution over the parameters, respectively. The evidence is therefore the prior-weighted average of the likelihood over the parameters. It gives the overall ability of the model to fit the data, rather than the power of any individual set of parameters. As is well known in statistics, and further described in Bailer-Jones (2011a), this is the appropriate metric to use in order to compare models of different flexibility or complexity.

If t_j is the *true* (unknown) time of the impact of crater j^{th}, and τ_j is the *measured* time with corresponding uncertainty σ_j, then an appropriate error model for this measurement is

$$P(\tau_j|\sigma_j, t_j) = \frac{1}{\sqrt{2\pi}\sigma_j} \exp[-(\tau_j - t_j)^2/2\sigma_j^2]. \qquad (16)$$

The likelihood for one crater measurement can then be calculated by integrating over the unknown time

$$
\begin{aligned}
P(\tau_j|\sigma_j, \theta, M) &= \int_{t_j} P(\tau_j|\sigma_j, t_j, \theta, M)P(t_j|\sigma_j, \theta, M)dt_j \\
&= \int_{t_j} P(\tau_j|\sigma_j, t_j)P(t_j|\theta, M)dt_j. \qquad (17)
\end{aligned}
$$

The second term in the second equation describes the time series model: it predicts the probability that an event will occur at time t_j given the parameters for that model. The likelihood for the whole time series, $D = \{\tau_j\}$, is the product of the individual likelihoods (assuming they are measured independently), in which case

$$P(D|\theta, M) = \prod_j P(\tau_j|\sigma_j, \theta, M). \qquad (18)$$

We use this in equation 15 to calculate the evidence for model M give the set of cratering dates. The absolute scale of the evidence is unimportant: we are only interested in ratios of the evidence for any pair of models, known as the *Bayes factor*. As a rule of thumb, if the Bayes factor is larger than 10, then the model represented in the numerator of the ratio is significantly favoured by the data over the other model (see Kass & Raftery (1995) for further discussion of the interpretation).

4.2 Time series models

The time series model, M, is a model which predicts the variation of the impact probability with time (the normalized cratering rate), i.e. the term $P(\tau_j|\sigma_j, \theta, M)$ in equation 18. The models we use in this work, along with their parameters, θ, are defined in Table 4, and described below

Uniform. Constant impact probability over the range of the data. As any probability distribution must be normalized over this range, this model has no parameters.

RandProb, RandBkgProb. Both models comprise N impact events at random times, with each event modelled as a Gaussian. N times are drawn at random from a uniform time distribution extending over the range of the data. A Gaussian is placed at each of these with a common standard deviation (equal to the average of

the real crater age uncertainties). We then sum the Gaussians, add a constant background, B, and normalize. This is the RandBkgProb ("random with background") model. RandProb is the special case for $B = 0$. We calculate the evidence by averaging over a large number of realizations of the model (i.e. times of the events), and, for RandBkgProb, over B. For example, when we later model the basic150 time series, we fix $N = 32$ and range B from 0 to ∞ (see Table 5).

SinProb, SinBkgProb. Periodic model of angular frequency ω and phase ϕ_0 (model SinProb). There is no amplitude parameter because the model is normalized over the time span of the data. Adding a background B to this simulates a periodic variation on top of a constant impact rate (model SinBkgProb).

SigProb. A monotonically increasing or decreasing nonlinear trend in the impact PDF using a sigmoidal function, characterized by the steepness of the slope, λ, and the center of the slope, t_0. In the limit that λ becomes zero, the model becomes a step function at t_0, and in the limit of very large λ it becomes the Uniform model. We restrict $\lambda < 0$ in our model comparison because the decreasing trend in cratering rate towards the past seems obvious in the time series (see Figure 1; see also Bailer-Jones (2011a)). However, we do include the increasing trend in our sensitivity test in Section 8.

SinSigProb. Combination of SinProb and SigProb.

TideProb, EncProb, EncTideProb. Models arising from the dynamical simulation of cometary orbits perturbed by either stellar encounters (EncProb) or the Galactic tide (TideProb) or both (EncTideProb). We describe the modelling approach which produces these distributions in detail in Section 5.

EncSigProb, TideSigProb, EncTideSigProb. Combination of EncProb, TideProb, EncTideProb (respectively) with SigProb.

Some of these models – those in the first five lines in Table 4 – are simple analytic models. The others are models based on dynamical simulations of cometary orbits, which we therefore call dynamical models. In the next section we will explain how we get from a simulation of the perturbation of the cometary orbits to a prediction of the cratering rate. Table 4 also lists the parameters of the models, i.e. those parameters which we average over in order to calculate the evidence. The prior distributions for these parameters are listed in Table 5.

5 MODELLING THE HISTORY OF THE COMETARY IMPACT RATE

The terrestrial impact rate consists of two parts: the asteroid impact rate and the comet impact rate. We are specifically interested in only the latter in the present work. The background asteroid impact rate is proportional to the number of asteroids in the asteroid belt, which is depleted by the impact of asteroids on planets and their satellites. Over a long time scale (longer than 100 Myr), the background impact rate of asteroids would therefore decrease towards the present. But we could also see variations in this due to the disruption of large asteroids into an asteroid family, which would produce phases of enhanced impacting (Bottke, David & David 2007). In addition to the actual impact rate, the geological record of all impact craters (comet or asteroid) is contaminated by a selection bias: The older a crater is, the more likely it is to have been eroded and so the less likely it is to be discovered. This preservation bias would lead to an apparent increase in the impact rate towards to the present. We model the combined contribution of these two components (variable asteroid impact rate and the preservation bias) to the measured impact rate using a sigmoidal function, which produces

a smoothly varying trend with time (model SigProb in Table 4). As with the other models, this model has parameters which we average over when computing the model evidence.

The cometary impact rate is determined by the gravitational perturbations of the Oort cloud due to the Galactic tide and stellar encounters. Both are modulated by the solar motion around the Galactic center. Some studies suggest that their combined effect injects more comets into the inner solar system than does each acting alone (Heisler, Tremaine & Alcock 1987; Rickman et al. 2008). This so-called synergy effect is difficult to model, however, and will be ignored in our statistical approach.

We simulate the effects of the tide and encounters separately (section 3). The resulting cometary flux from these is described by the models TideProb and EncProb respectively. The cometary flux when both processes operate, the model EncTideProb, is the sum of the fluxes from each (each being normalized prior to combination). To include the contributions from the asteroid impacts and the crater preservation bias we can add to this the SigProb model mentioned above. This gives the model EncTideSigProb. The parameters of all these models and their prior ranges are defined in Tables 4 and 5.

5.1 Tide-induced cometary flux

The time variation as the Sun orbits the Galaxy of the tide-induced cometary flux entering the loss cone is calculated using AMUSE-based method (section 3.4). We define f_c as the relative injected comet flux in a time bin with width Δt

$$f_c = \frac{N_{\text{inj}}}{N_{\text{tot}} \Delta t}, \tag{19}$$

where N_{inj} is the number of injected comets in this bin and N_{tot} is the total number of the comets.

We could use f_c directly as the model prediction of the comet impact cratering rate, $P_u(t|\theta, M)$, for the model TideProb (section 4.2) for that particular set of model parameters. However, as the calculation of the cometary orbits is rather time-consuming, we instead use a proxy for f_c, i.e. the vertical tidal force.

The tidal force per unit mass experienced by a comet in the Oort Cloud is

$$\mathbf{F} = -\frac{GM_\odot \, \hat{\mathbf{r}}}{r^2} - G_1 x \, \hat{\mathbf{x}} - G_2 y \, \hat{\mathbf{y}} - G_3 z \hat{\mathbf{z}} \tag{20}$$

where $\mathbf{r}$ is the Sun-comet vector of length r, $M_\odot$ is the solar mass, and G is the gravitational constant.[5] The three tidal coefficients, G_1, G_2, and G_3 are defined as

$$\begin{aligned} G_1 &= -(A - B)(3A + B) \\ G_2 &= (A - B)^2 \\ G_3 &= 4\pi G \rho(R, z) - 2(B^2 - A^2) \end{aligned} \tag{21}$$

where A and B are the two Oort constants, and $\rho(R, z)$ is the local mass density which can also be denoted as $\rho(t)$ in the case of using $G_3(t)$ to build models. Because the two components G_1 and G_2 in the Galactic (x, y) plane are about ten times smaller than the vertical component (G_3), it is the vertical tidal force that dominates the perturbation of the Oort Cloud.

To find a relationship between f_c and G_3, we simulate the orbits of one million comets generated from the DQT model back to

---

[5] We don't use this equation in simulating cometary orbits in the AMUSE framework.

Table 4. The mathematical form of the time series models and their corresponding parameters. Time t increases into the past and $P_u(t|\theta, M)$ is the unnormalized cratering rate (probability density) predicted by the model. In the dynamical models (EncProb, TideProb, EncTideProb, EncSigProb, TideSigProb, and EncTideSigProb), $\vec{r}_\odot(t = 0Myr)$ and $\vec{v}_\odot(t = 0Myr)$ are Sun's current position and velocity relative to the Galactic center. Note that the components in the compound models are normalized before being combined. The quantities $\gamma_{\rm bin}(t)$, $G_3(t)$, and ξ are defined in Section 5. η is a parameter which describes the relative contribution of the two combined models.

model name	$P_u(t|\theta, M)$	parameters, θ
Uniform	1	none
RandProb/RandBkgProb	$\sum_{n=1}^{N} \mathcal{N}(t; \mu_n, \sigma) + B$	σ, B,N
SinProb/SinBkgProb	$1/2\{\cos[\omega t + \phi_0] + 1\} + B$	ω, β, B
SigProb	$[1 + e^{(t-t_0)/\lambda}]^{-1}$	λ, t_0
SinSigProb	SinProb+SigProb	T, β, B,λ, t_0
EncProb	$\gamma_{\rm bin}(t)$	$\vec{r}_\odot(t = 0)$, $\vec{v}_\odot(t = 0)$
TideProb	$G_3(t)$	$\vec{r}_\odot(t = 0)$, $\vec{v}_\odot(t = 0)$
EncTideProb	$[\gamma_{\rm bin}(t) + \xi G_3(t)]/(1 + \xi)$	ξ, $\vec{r}_\odot(t = 0)$, $\vec{v}_\odot(t = 0)$
EncSigProb	EncProb + η SigProb	η, λ, t_0, $\vec{r}_\odot(t = 0)$, $\vec{v}_\odot(t = 0)$
TideSigProb	TideProb + η SigProb	η, λ, t_0, $\vec{r}_\odot(t = 0)$, $\vec{v}_\odot(t = 0)$
EncTideSigProb	EncTideProb + η SigProb	ξ, η, λ, t_0, $\vec{r}_\odot(t = 0)$, $\vec{v}_\odot(t = 0)$

Table 5. The prior distribution and range of parameters for the various time series models. For the non-dynamical models (i.e. all except the last five lines), a uniform prior for all the parameters is adopted which is constant inside the range shown and zero outside. $N_{\rm ts}$ and $\tau_{\rm max}$ are the number of events and the earliest time of occurrence of the craters. $\bar{\sigma}_i$ is the averaged age uncertainties of the craters. The prior PDFs over the parameters of the dynamical models (the last five lines) are Gaussian, with means and standard deviations set by the initial conditions as listed in Table 3.

model name	details of the prior over the parameters
Uniform	no parameters
RandProb	$\sigma = \bar{\sigma}_i$, $N = N_{\rm ts}$, $B = 0$
RandBkgProb	$\sigma = \bar{\sigma}_i$, $N = N_{\rm ts}$, $B = \frac{1}{\sqrt{2\pi}\sigma}\frac{b}{(1-b)}$ with $b \in [0, 1]$
SinProb	$2\pi/100 < \omega < 2\pi/10, 0 < \phi_0 < 2\pi, B = 0$
SinBkgProb	$2\pi/100 < \omega < 2\pi/10, 0 < \phi_0 < 2\pi, B = \frac{b}{(1-b)}$ with $b \in [0, 1]$
SigProb	$-100 < \lambda < 0, 0 < t_0 < 0.8\tau_{\rm max}$
SinSigProb	Priors from both SinProb and SigProb
EncProb	Initial conditions listed in Table 3
TideProb	Initial conditions listed in Table 3
EncTideProb	$\xi = 1$, Initial conditions listed in Table 3
EncSigProb	$0 < \eta < 4, -100 < \lambda < 0, 0 < t_0 < 0.8\tau_{\rm max}$, initial conditions listed in Table 3
TideSigProb	$0 < \eta < 4, -100 < \lambda < 0, 0 < t_0 < 0.8\tau_{\rm max}$, initial conditions listed in Table 3
EncTideSigProb	$\xi = 1, 0 < \eta < 4, -100 < \lambda < 0, 0 < t_0 < 0.8\tau_{\rm max}$, initial conditions listed in Table 3

1 Gyr in the past under the perturbation of the Galactic tide (stellar encounters are excluded). We use here the loss cone as the target zone when identifying the injected comets (LPCs). The two quantities are compared in Figure 10. We see that the detrended comet flux (red line) agrees rather well with G_3 (blue line) over the past 1 Gyr, albeit with an imperfect detrending over the first 100 Myr. We made a similar comparison for the DLDW model and also find a very close linear relation. Comparing G_3 with the flux of the comets injected into the observable zone (i.e. $q < 5$ AU) for both the DLDW and DQT models, we find that the result is consistent with what we have found for the loss cone. This confirms the relationship between the tide-induced comet flux and the vertical tidal force, which was also demonstrated by Gardner et al. (2011) (their Figure 9) with a different approach. We are therefore justified in using G_3 as a proxy for the tide-induced comet flux when we build models of cometary impact rate to compare to the crater time series.

5.2 Encounter-induced cometary flux

We define the encounter-induced flux entering the loss cone in the same way as f_c in equation 19. We now investigate whether we can introduce a proxy for this too. We postulate the use of the quantity

$$\gamma = \frac{M_{\rm enc}}{v_{\rm enc} r_{\rm enc}} \tag{22}$$

which is proportional to the change in velocity of the Sun (or equivalently to the mean change in velocity of the comets) as induced by an encounter according to the classical impulse approximation (Oort 1950; Rickman 1976). This proxy has also been used in previous studies to approximate the LPC flux injected by stellar encounters (e.g. Kaib & Quinn (2009); Fouchard et al. (2011)).

The injected flux is dominated by those encounters which can signifcantly change the velocity and thus the perihelion of the comets (Hills 1981; Heisler, Tremaine & Alcock 1987; Fouchard et al. 2011). Considering the important role of these encounters and the long time scale between them (about 100 Myr according to Heisler, Tremaine & Alcock 1987), we divide the whole time span of simulated stellar encounters into several time bins and use the (normalized) maximum value of γ in each bin to approxi-
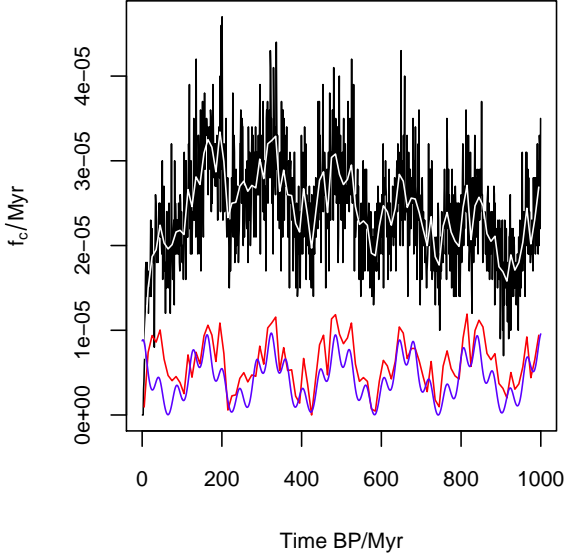
Figure 10. Comparison between the tide-induced injected comet flux (f_c) and the vertical Galactic tide (G_3). The injected comet flux is shown as a histogram with two different bins sizes: 1 Myr (black line) and 10 Myr (white line). The red line is the detrended comet flux with a time bin of 10 Myr. The blue line shows the variation of G_3 (scaled, as it has a different unit to f_c).
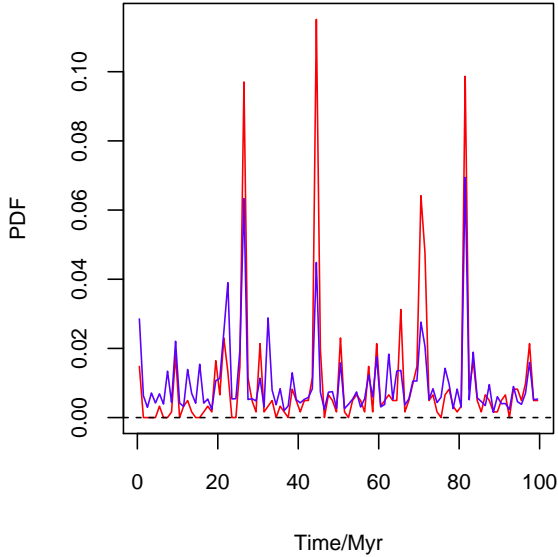

Figure 11. The time-varying probability density of the encounter-induced injected comet flux f_c (red line) and the prediction of proxy $\gamma_{\rm bin}$ (blue line), binned with a time bin of 1 Myr.

mate such comet showers. We define this binned proxy as $\gamma_{\rm bin}$, and normalize it over the whole time scale. In Figure 11, we compare this proxy to the normalized encounter-induced flux which is simulated with a time step of 0.001 Myr using a sample of 10^5 comets generated from the DLDW model over 100 Myr. We find that the main comet showers can be properly predicted by $\gamma_{\rm bin}$, although it
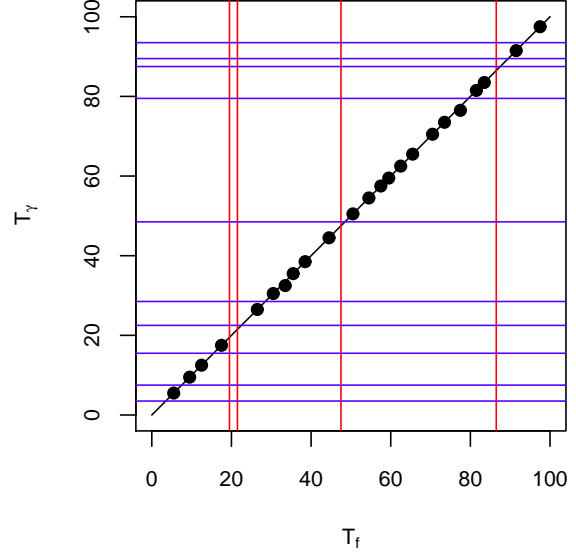

Figure 12. Assessment of the comet shower prediction ability of the proxy γ. The black points show peaks which are correctly reproduced, by plotting their time of occurrence in the proxy, T_γ, against their true time of occurrence, T_f, in f_c. Peaks missed by the proxy are shown as vertical red lines and false peaks in the proxy are shown as horizontal blue lines.

may miss small comet showers and predict some non-existent small showers.

To assess the reliability of the shower prediction of the proxy, we evaluate the fraction of peaks in f_c which are correctly identified by $\gamma_{\rm bin}$, and the fraction of peaks in $\gamma_{\rm bin}$ which have a corresponding true peak in f_c. For the former case, a peak in f_c is counted as correctly predicted by the proxy when it occurs in the same time bin as a peak in $\gamma_{\rm bin}$, or when the f_c peak is one bin earlier (because the shower can occur up to 1 Myr after the closest approach of the encounter). We find that 23 out of 27 (0.85) flux peaks are correctly predicted by the proxy, while 23 out of 33 (0.70) peaks in $\gamma_{\rm bin}$ have corresponding peaks in f_c (Figure 12). This simple counting ignores the intensity of the comet showers. To remedy this use the amplitude of each $\gamma_{\rm bin}$ peak as a weight, and count the weighted fractions. We find these to be 0.92 and 0.84 respectively. These results suggests that $\gamma_{\rm bin}$ is a reasonably good proxy for statistical purposes. Hence we use $\gamma_{\rm bin}$ as the measure of $P_u(t|\theta, M)$ for the model EncProb. The linear relationship between $\rho(t)$ and $G_3(t)$ (equations 9 and 21) indicates that the averaged EncProb model over sequences of $\gamma_{\rm bin}$ is equivalent to the corresponding TideProb model for one solar orbit. We will see in section 6 whether there is any significant difference between the evidences for these two models.

5.3 Combined tide–encounter cometary flux

Having defined TideProb and EncProb, we can combine them to make EncTideProb. We can further combine this sum with Sig-Prob (scaled by the parameter η) in order to include a smoothly varying component (see Table 4). Figure 13 shows examples of the TideProb, EncTideProb and EncTideSigProb model predictions of the cometary flux for specific values of their parameters. In the upper panel, we see the TideProb model predicts an oscillating variation on at least two time scales. In the middle panel, we add
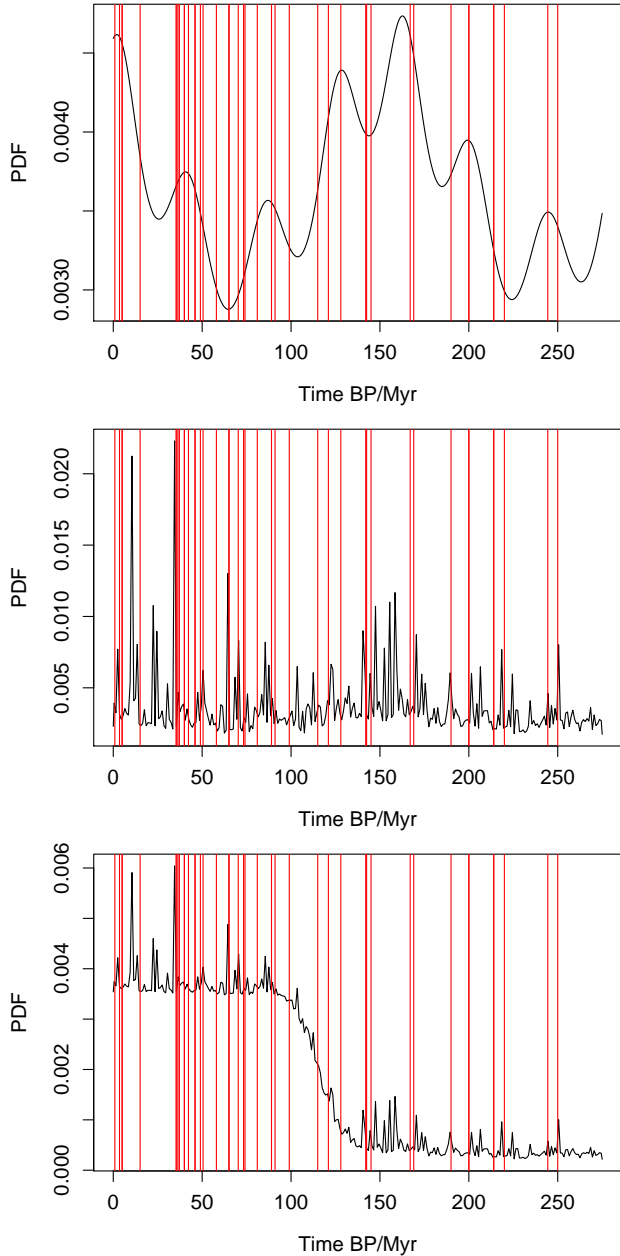
Figure 13. The prediction of the normalized cometary impact rate (i.e. probability density function; black line) compared to the actual impacts in the basic250 time series (red lines). The models from top to bottom are TideProb, EncTideProb, and EncTideSigProb. A common solar orbit and encounter sample is used in all three cases.

EncProb to TideProb. The amplitude of the background is reduced due to the normalization effect – the encounters dominate – and the high peaks characterize encounter-induced comet showers. In the bottom panel, the SigProb model is added onto the EncTideProb model with $\eta = 3$. A large value of λ has been used in SigProb here, such that the additional trend is almost linear. Meanwhile, we also combine TideProb and SigProb to make TideSigProb. This of course does not show the randomly occurring peaks which are characteristic of the encounters model.

In Section 6, we will compare these models with other time series models defined in Section 4.2 using Bayesian method.

6 MODEL COMPARISON

Now that we have a way to generate predictions of the comet flux from our dynamical time series models, we use the Bayesian method described in section 4 to calculate the evidences for the various time series models defined in section 4.2 for different cratering data sets. Because the solar orbit is more sensitive to the Sun's initial galactocentric distance (R) and angular velocity ($\dot{\phi}$) than to the other four initial conditions (Feng & Bailer-Jones 2013), we sample over only those two parameters when calculating the evidences and Bayes factors (ratio of two evidences) for the dynamical models. In order to make our model comparison complete, we will vary all initial conditions individually and simultaneously in section 8.

To calculate the evidences we sample the parameter space of the dynamical models and other time series models with 10^4 and 10^5 points respectively. For the models of EncProb, EncTideProb, EncSigProb and EncTideSigProb, each point represents an entire simulation of the orbit of the Sun about the Galaxy and the corresponding simulation of the comet flux as a function of time. For the latter we use the proxies of $G_3(t)$ and $\gamma(t)$ (i.e. the time-varying γ_{bin}) described in section 5.1 and section 5.2 respectively. For each orbit of the Sun we just generate a single sequence $\gamma(t)$ for the comet flux at random. (Because $\gamma(t)$ is modulated by the vertical tide coefficient $G_3(t)$, an average over many sequences of $\gamma(t)$ would be smooth and lack the spikes corresponding to comet showers which we see in the individual sequences.)

The Bayes factors of various models relative to the uniform model are listed in Table 6. We see that the SigProb, EncSigProb, TideSigProb and EncTideSigProb models are favoured by all the data sets, sometimes marginally, sometimes by a significant amount relative to certain models. In these favoured models, the negative trend (a decreasing cratering rate towards the past) is favoured much more than the positive trend. Such a negative trend can be picked out in Figure 1. As the positive values are so clearly ruled out, we only use negative values of λ in all the trend models. This would be consistent with the crater preservation bias or the disruption of a large asteroid dominating over any recent increase in the asteroid impact rate (see section 5).

The SinSigProb model is not favoured more than SigProb, which means the periodic component is not necessary in explaining cratering time series. This is consistent with the conclusion in Bailer-Jones (2011a). Moreover, the pure periodic model is actually slightly less favoured than the uniform model for the "basic" and "ext" data sets. The pure random model (RandProb) is slightly more favoured than the random model with background (RandBkgProb). Both are more favoured than the uniform model, but with relatively low Bayes factors compared to the models with trend components.

EncProb is slightly more favoured than the TideProb model. This suggests that the stochastic component of EncProb is slightly preferable to the smooth tidal component of TideProb in predicting the cratering data, although the difference is small. Combining them to make the EncTideProb models does not increase the evidence.

The best overall model for explaining the data is SigProb, the pure trend model. Adding the tide or encounters or both does not increase the evidence by a significant amount for any of the data sets. This suggests that the solar motion has little influence on the total observed impact rate (i.e. comets plus asteroids and the preservation bias) either through the Galactic tide or through stellar encounters, at least not in the way in which we have modelled them here. This minor role of the solar motion in generating terres-

Table 6. Bayes factors of the various time series models (rows) relative to the uniform model for the various data sets (columns). The suffix numbers 1 and 2 in the model names, e.g. EncProb1 and EncProb2, refer to which different initial conditions are fixed. 1 means $R(t = 0)$ and 2 means $\dot{\phi}(t = 0)$.

Model	basic150	ext150	full150	basic250	ext250	full250
RandProb	4.4	9.3	72	3.0	9.4	4.7×10^2
RandBkgProb	1.8	3.8	31	2.2	5.2	1.8×10^2
SinProb	0.34	0.62	1.2	0.43	0.76	1.5
SinBkgProb	1.0	1.2	1.6	1.0	1.2	1.5
SigProb	15	63	9.1×10^3	2.0×10^2	1.8×10^3	5.8×10^6
SinSigProb	10	36	1.6×10^2	1.0×10^2	6.0×10^2	2.6×10^5
EncProb1	1.5	3.9	26	1.7	5.2	1.1×10^2
EncProb2	1.7	3.3	77	1.6	8.5	2.7×10^2
TideProb1	0.73	0.87	6.7	0.81	0.91	1.1
TideProb2	0.79	0.86	10	0.69	0.76	0.94
EncTideProb1	1.0	1.6	18	1.3	2.1	10
EncTideProb2	1.2	1.8	25	1.2	2.1	24
EncSigProb1	11	41	4.6×10^3	1.5×10^2	1.5×10^3	5.9×10^6
EncSigProb2	12	52	8.7×10^3	1.7×10^2	1.5×10^3	6.6×10^6
TideSigProb1	11	38	4.6×10^3	1.6×10^2	1.4×10^3	6.2×10^6
TideSigProb2	10	37	4.5×10^3	1.6×10^2	1.4×10^3	6.1×10^6
EncTideSigProb1	11	40	5.0×10^3	1.6×10^2	1.4×10^3	6.0×10^6
EncTideSigProb2	11	40	4.7×10^3	1.6×10^2	1.5×10^3	6.1×10^6

trial craters weakens the hypothesis that the (semi-)periodic solar motion triggers mass extinctions on the Earth through modulating the impact rate, as some have suggested (Alvarez & Muller 1984; Raup & Sepkoski 1984). We note that a low cometary impact rate relative to the asteroid impact rate has been found by other studies (Francis 2005; Weissman 2007).

The evidence is the prior-weighted average of the likelihood over the parameter space. It is therefore possible that some parts of the parameter space are much more favoured than others (i.e. there is a large variation of the likelihood), and that this is not seen due to the averaging. In that case changing the prior, e.g. the range of the parameter space, could change the evidence. (We investigate this systematically in section 8). In other words, the tide or encounter models may play a more (or less) significant role if we had good reason to narrow the parameter space. This would be appropriate if we had more accurate determinations of some of the model parameters, for example. We now investigate this by examining how the likelihood varies as a function of individual model parameters (but still be averaged over the other model parameters).

Figure 14 shows how the resulting likelihood varies as a function of the four parameters in the TideSigProb1 model. The most favoured parameters of the trend component are $\lambda \approx -60\,\mathrm{Myr}$ and $t_0 \approx 100\,\mathrm{Myr}$. This trend component represents an increasing cratering rate towards the present over the past 100 Myr (Shoemaker 1998; Gehrels, Matthews & Schumann 1994; McEwen, Moore & Shoemaker 1997), either real or a result of preservation bias. In the upper left graph, the likelihood varies with R slightly and varies a lot in the region where $R < 8\,\mathrm{kpc}$ and $R > 9\,\mathrm{kpc}$. In the lower right panel, the likelihood increase with η, which means that the trend component is important in increasing the likelihood for the TideSigProb model.

To find the relationship between the likelihood for TideSigProb and the Sun's initial galactocentric distance R and the scale parameter η, we fix the parameters of the trend component to $\lambda = -60\,\mathrm{Myr}$ and $t_0 = 100\,\mathrm{Myr}$. In Figure 15 we see that the likelihood for TideSigProb increases monotonically with η over this range, but has a more complex dependence on R. The likelihood is highest at around $R = 7.0$ and $R = 9.5\,\mathrm{kpc}$. In Figure 16 we
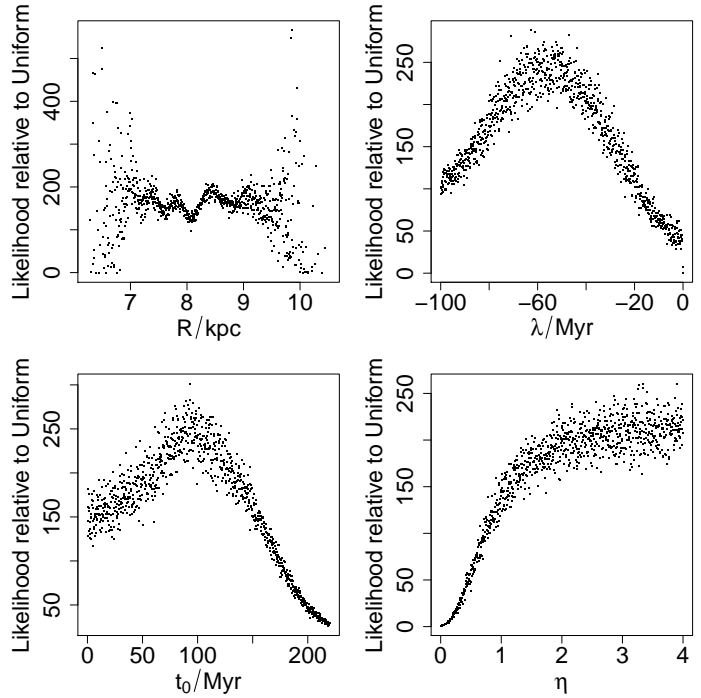
Figure 14. The distribution of the likelihood over each of the parameters in the TideSigProb1 model for the basic250 data set, sampling over all other parameters in each case. The parameters are divided into 1000 bins. For each bin, the likelihoods are averaged to reduce the noise generated by the randomly selected sequence of stellar encounters. There are 100 000 samples in the parameter space.

compare the dates of the craters in the basic250 data set with the prediction of the cratering rate from TideProb with $R = 7.0\,\mathrm{kpc}$. There are 7 craters within the first 30 Myr compared to 16 and 13 craters in the intervals [30,60] Myr and [60,90] Myr respectively. This lack of craters in the first 30 Myr can be better predicted by
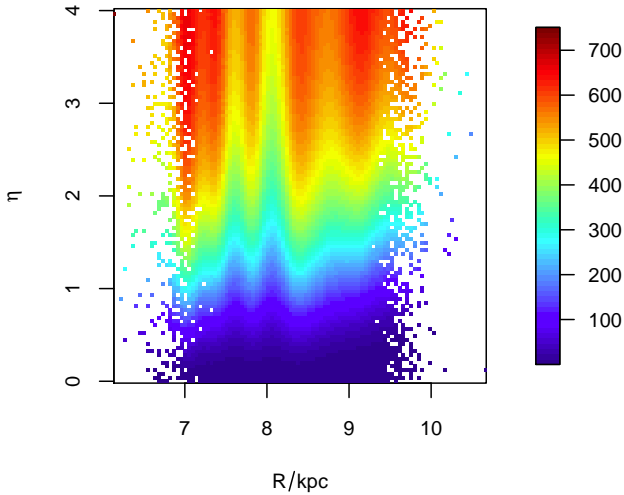
Figure 15. The distribution of the likelihood over the parameters R and η in the TideSigProb1 model relative to the Uniform model for the basic250 data set. The relative likelihood is shown as the colour scale indicated in the legend. There are 100 000 samples in the parameter space.
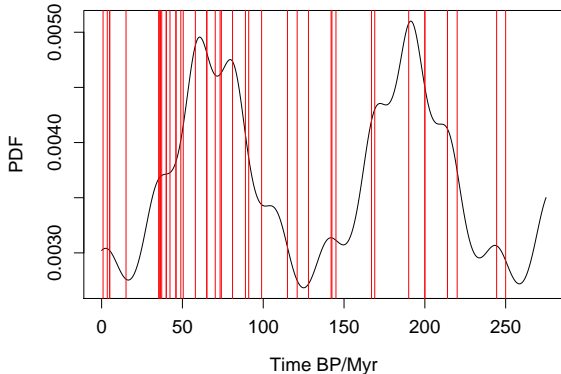

Figure 16. Comparison between the prediction of TideProb with $R = 7.0$ kpc (shown as a probability distribution function in black) and the times of the impact craters in the basic250 data set (shows as vertical red lines).

TideSigProb than by the SigProb model with a negative λ. While this is small number statistics, it may suggest that even though we have little evidence for the effect of the tide on cometary impacts in the overall cratering data, it may have had more of an effect in selected time periods. Other explanations are also possible, of course: we cannot say anything about models we have not actually tested, such as a more complex model for the asteroid impact rate variation.

7 MODELLING THE ANGULAR DISTRIBUTION OF COMETARY PERIHELIA

In this section we predict the 2D angular distribution (latitude, longitude) of the perihelia of LPCs, the observed data for which are shown in Figure 2. To do this we need to identify from the simulations comets injected over an appropriate time scale. Figure 11 shows that a comet shower usually has a duration of less than

10 Myr, something which was also demonstrated by Dybczyński (2002) in detailed simulations of individual encounters. The Galactic tide varies little over such a time scale, because the vertical component of the tide, which dominates the total Galactic tide, varies over the period of the orbit of the Sun about the Galaxy, which is of order 200 Myr. We may therefore assume that the solar apex is also more or less fixed during the past 10 Myr, which is then an appropriate time scale for constructing our sample.

We simulate cometary orbits over the past 10 Myr as follows: (1) generate one million comets from the Oort cloud model (DLDW or DQT), as well as a set of stellar encounters (about 400 over 10 Myr); (2) integrate the cometary orbits under the perturbations of only the Galactic tide (tide-only simulations with a time step of 0.1 Myr), only stellar encounters (encounter-only simulations with a time step of 0.01 Myr), and both of them (combined simulations with a time step of 0.01 Myr) back to 10 Myr ago; (3) identify the injected comets and their longitudes and latitudes. We then repeat steps (1)–(3) ten times (i.e. resample the Oort cloud and the set of stellar encounters) and combine the results in order to increase the number statistics.

7.1 Latitude distribution

The upper panels of Figure 17 compare the Galactic latitudes of the LPC perihelia with our model predictions. In addition to showing the model predictions for the comets injected into the loss cone, we also show the predicted distributions for comets injected into the observable zone ($q < 5$ AU). The former contains more comets, but the latter is of course closer to the observed sample. The small sample of comets within the observable zone have significant sample noise in their angular distributions, so we will only compare model predictions of the angular distribution of comets in the (larger) loss cone.

The upper panels show that the injected LPCs in the pole and equatorial regions are depleted for both DLDW and DQT models, as also found by Delsemme (1987). According to theoretical prediction, the tide-induced flux should be proportional to $|\sin b \cos b|$ (Matese, Whitman & Whitmire 1999), in very good agreement with our tide-only simulations. The observed data broadly agree with this, the main difference being that for negative latitudes the peak is at around -0.4 rather than the model-predicted value of -0.7. This discrepancy was also noticed by Matese & Whitmire (2011), for example, and could be a consequence of the small size of the data set (note the errors bars in the figure).

We see in the figure that the PDF of the latitude distribution predicted by the combined simulation always lies between those predicted by the single perturbation simulations. Although the combined simulation of comets injected into the loss cone predicts a flatter distribution than the tide-only simulation does, the stellar encounters cannot entirely smooth out the peaks in the latitude distribution. This is consistent with the results in Rickman et al. (2008). Thus the observed non-uniform latitude distribution does not indicate that the Galactic tide dominates at the present epoch, as was claimed by Matese & Whitmire (2011).

We can attempt to make a more quantitative assessment of how well our models predict the observed distribution. Using model comparison techniques we can ask whether our dynamical models (the combined tide plus encounters model) explain the data better than a uniform distribution. We can do this crudely on the binned data/simulations shown in the figure via a likelihood test. The act of binning means that the model-predicted number of events per bin is determined by the Poisson distribution, thus defin-
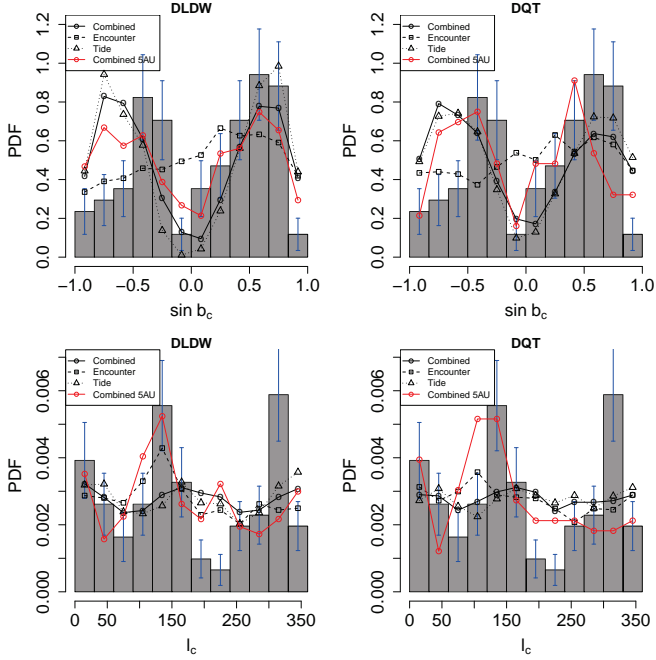
Figure 17. Comparison between the observed distribution (histogram blocks) and model-predicted distributions (points/lines) of the perihelia of long-period comets (LPCs) with Galactic latitude (upper panels) and longitude (lower panels) for the DLDW (left panels) and the DQT (right panels) Oort cloud initial conditions. All distributions are normalized. The error bars on the data have been calculated using a Poisson noise model (arising from the binning) with a total of 102 class 1A LPCs. The model-predicted distributions show the comets injected into the loss cone for three modes of simulations, namely including only the Galactic tide (triangles), only stellar encounters (squares), and both (circles). The number of injected comets in these simulations for the DLDW (DQT) models are 1858 (981), 1133 (1976), and 12751 (2796), respectively. The red circles connected by red lines show the number of comets injected into the observable zone ($q < 5$ AU), and comprise 449 comets for the DLDW model, and 112 for the DQT model.

ing our likelihood. However, such a test is dependent on the choice of binning, and we have tried out a range of bin widths and centres. While we find that the combined model for the DQT Oort cloud model is always more favoured than a uniform distribution, the significance is marginal.

An alternative approach is to use the unbinned data and unbinned model predictions, and to apply a kernel density estimate (KDE) to each. This produces a non-parametric density function for the data and for the model, the difference between which we quantify using the (symmetrized) Kullback-Leibler divergence (KLD). A value of zero divergence means that the two distributions are identical; larger (positive/negative) values indicate larger differences. We find that our dynamical models give smaller KLD values than do the uniform model (i.e. the former predict the data better), for both the DLDW and DQT. Although the distributions formed by the KDE are sensitive to size of the kernel adopted,[6] we find that

---

[6] This is analogous to the size of the histogram bins. A histogram is just a particular type of kernel.

the KLD values are quite insensitive to this, and consistently favour the dynamical models. This suggests that the dynamical models explain the data better than a flat distribution in latitude (although because calibrating KLD ratios into formal significances is not easy, we leave this as a qualitative statement).

7.2 Longitude distribution

The perihelia of LPCs are not distributed uniformly on the celestial sphere. It has been suggested (Matese, Whitman & Whitmire 1999; Matese & Whitmire 2011) that they lie preferentially on a great circle, as evidenced by two peaks at $l_c \simeq 135°$ and $l_c \simeq 315°$ seen in Figure 2. The comets on this great circle could be induced by stellar encounters with preferred directions, thereby producing the apparent anisotropy. In the lower two panels in Figure 17, we see that the model predictions do not produce any very large peaks, although one around $l_c \simeq 135°$ is discernable. We also observe a peak around $l_c = 0$–$60°$ which is proposed as a signal of the "Biermann comet shower" (Biermann, Huebner & Lust 1983; Matese, Whitman & Whitmire 1999). In our model, this peak is probably the result of accumulated perturbations from several stellar encounters with preferred directions.

The peak around $l_c = 135°$ is more prominent in the model prediction for the comets injected into the observable zone (red points/line in the figure). This peak is generated primarily by one or more massive stellar encounters. Hence, stellar encounters play a more significant role in injecting comets into the observable zone than just into the loss cone. This is consistent with the "synergy effect" investigated by Rickman et al. (2008).

As with the latitude distribution, we also measured the KLD for the model predictions (for the loss cone) and for a uniform distribution. The dynamical models predict the data little better than a uniform distribution. (The likelihood test gives a similar result.) One reason for this lack of support for our dynamical (combined) model could be the fact that we are averaging the predicted distribution from the encounters over ten different realizations of the stellar encounters. This will tend to smooth out individual peaks, which are probably produced by just a few encounters with massive stars.[7] If we instead only used a single random realization of encounters, we are unlikely to reproduce exactly the showers which occurred. This is an inherent problem of modelling stellar encounters in a stochastic way. This does not affect our model prediction of the latitude distribution nearly as much, however, because its shape is dominated by the non-stochastic tide.

In order to investigate this we again use our encounter model via the proxy γ (a proxy of comet flux) defined in equation 22, but now as a function of b_p and l_p, the direction toward the perihelion of the stellar encounter. Moreover, we now impose a minimum threshold, $\gamma_{\lim}$, on the proxy: The larger the value of $\gamma_{\lim}$, the larger the encounter perturbation must be for it to be included in the model.

Using the encounter model described in section 3.3, we simulate 10 million encounters and calculate γ, b_p, and l_p for each. The predicted direction of an LPC's perihelion is opposite on the sky to the direction of the encounter perihelion. Thus we can calculate b_c and l_c accordingly and use $\gamma(b_c, l_c)$ to predict the PDF of b_c and l_c. Then we divide the range of the Galactic longitude

---

[7] Such massive stars (or stars with relatively high γ) move slowly relative to the Sun, and so would generate a relatively narrow peak in comet flux with l_c.
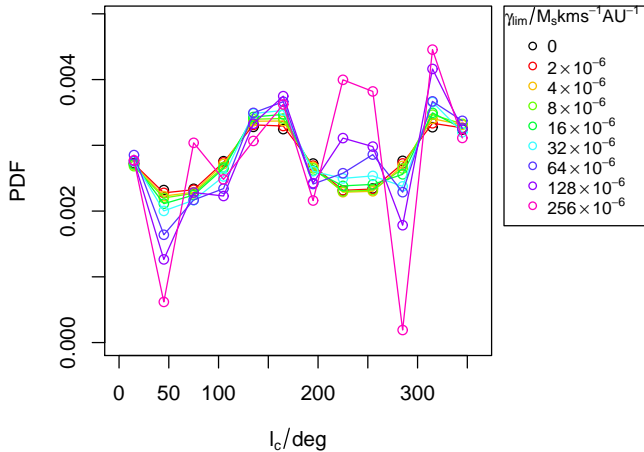
Figure 18. Predictions of the encounter-induced cometary flux when adopting different lower limits, $\gamma_{\lim}$, on the value of γ required for an event to have an influence on the Oort cloud. There are 10^7 and 10^8 encounters generated for the model predictions with $\gamma_{\lim} = 0$ and $\gamma_{\lim} \neq 0$ respectively.

into 12 bins and sum γ in each bin including only those encounters with $\gamma > \gamma_{\lim}$. Normalizing this gives the angular PDF of the encounter-induced flux, as shown in Figure 18. For larger values of $\gamma_{\lim}$ we observe a larger variation in the flux with longitude, as expected, because then fewer encounters contribute to the distribution. As we can see from equation 22, these are the more massive and/or slower stars. These encounters may induce a series of weak comet showers rather than a single strong comet shower. Because strong encounters are rare and extremely weak encounters cannot induce enough anisotropic LPCs, the spikes in the longitude distribution can be caused by at least two weak encounters rather than one strong or many extremely weak encounters. From Figure 17, we see that the tide cannot completely wash out the anisotropy in the longitude distribution induced by these encounters.

Consistent with our results, Matese & Whitmire (2011) found that the two spikes in the longitude distribution result from weak impulsive perturbations by analyzing the energy and angular momentum of dynamically new LPCs. Similar to the definition of weak comet showers in Matese & Lissauer (2002) and Dybczyński (2002), we define encounters with γ in the interval $[1 \times 10^{-7}, 5 \times 10^{-6}] M_\odot \ km \ s^{-1} \ AU^{-1}$ as weak encounters. We do not find strong peaks in the longitude distribution of γ for these encounters in Figure 18, because we know that γ can underestimate the intensity of the shower (see Figure 11). Thus a small enhancement of the two peaks in Figure 18 may correspond to a large enhancement of the peaks in the longitude distribution as predicted by our dynamical model in Figure 17.

Inspecting the catalogue of the frequencies of different types of stellar encounters in table 8 of García-Sánchez et al. (2001), we see that there were at least eight encounters with masses equal to or larger than one solar mass encountering the solar system in the past 10 Myr with perihelia less than 1 pc. These encounters can move to a heliocentric distance much larger than 50 pc over that time, which is the upper limit for their unbiased sample of stellar encounters with $M_V < 5$ – see Figure 13 of García-Sánchez et al. (2001).

We also point out that GL 710 will have a close approach with the solar system in about 1.4 Myr at a perihelion longitude of around 135°. According to studies, it will induce a weak comet shower which is expected to increase the cometary flux by 40%-

50% (García-Sánchez et al. 1999; Matese & Lissauer 2002). This supports the suggestion that the solar apex motion induces the non-uniform longitude distribution of the LPCs' perihelia (see Figure 6 and 17). In addition, Algol, a triple-star system with a total mass of $5.8 \, M_\odot$, encountered the solar system with a closest distance of 2.5 pc 6.9 Myr ago (García-Sánchez et al. 2001). The Galactic longitude of Algol was also close to $135°$.

Based on the above plausible scenario, we conclude that the peaks in the longitude distribution of LPC perihelia could arise from the perturbations of a few strong stellar encounters, the encounter directions of which depend on the solar apex motion. Considering the important role of the Galactic tide in generating a non-uniform latitude distribution, and the role of stellar encounters in generating a non-uniform longitude distribution, the synergy effect plays a role in maintaining – rather than smoothing out – the anisotropy in the observed LPCs. In other words, we can explain the anisotropy of the LPC perihelia based only on the solar apex motion and the Galactic tide, without needing to invoke the Jupiter-mass solar companion as proposed by Matese & Whitmire (2011). To date there is no observational evidence for such a companion. We note that a recent analysis of data from the WISE satellite has excluded the existence of a Jupiter-mass solar companion with a heliocentric distance less than 1 pc (Luhman 2014).

8 SENSITIVITY TEST

8.1 Spiral arms and Galactic bar

The spiral arms and Galactic bar are non-axisymmetric, time-varying components of the Galactic potential. These make only a small contribution to the tidal force acting on the Sun and Oort cloud (Binney & Tremaine (2008); Cox & Gómez (2002)). However, if their contribution is always in the same direction, the effect of their perturbation could accumulate. This can occur when the Sun is near to the co-rotation resonance, when the rotation velocities of the disk and of the spiral pattern coincide. To test this hypothesis, we simulate the solar and cometary motion adopting various constant pattern speeds of the spiral arms and the bar with fixed Galactic density distributions (specified in Section 3.1).

We integrate the solar orbit in the Galactic potential both including and excluding the non-axisymmetric components. The initial conditions of the Sun and potential parameters are given in Table 2. We find that the gravitational force from the bar is always much larger than that from the spiral arms. However, the difference between the pattern speed of the Galactic bar Ω_b and solar angular velocity is much larger than the difference between the pattern speed of the spiral arms Ω_s and solar angular velocity, which results in a much lower accumulated perturbation due to the bar. To see this effect, we integrate the solar orbit back to 5 Gyr in the past. The variations of galactocentric radius and vertical displacement of the Sun are shown in Figure 19. The arms have a stronger effect on the solar orbit than does the bar. The spiral arms tend to increase the galactocentric radius of the Sun as the integration proceeds (back in time), while the bar modulates the galactocentric radius by a comparatively small amount. Neither the bar nor the arms significantly affect the vertical displacement amplitude of the Sun. Here the combined perturbation from the potential including both the Galactic bar and spiral arms changes the solar motion the same way as the perturbation from the bar alone.

We now simulate the tide-induced flux corresponding to these different potential models. The lower panel in Figure 20 shows that
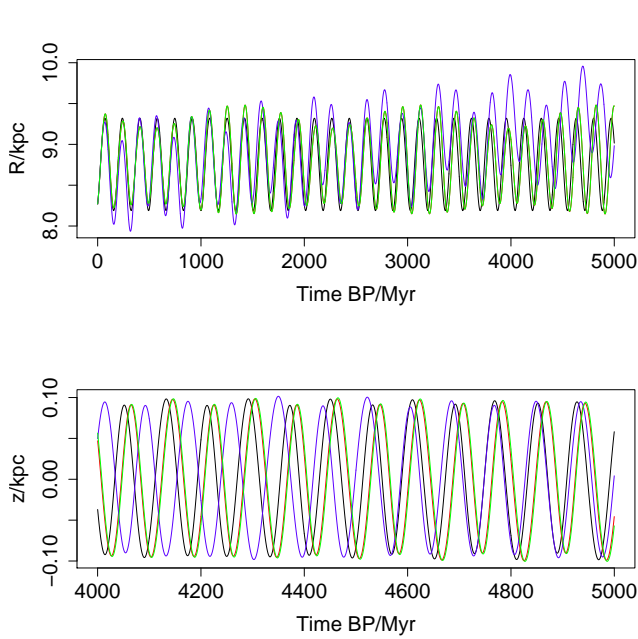
Figure 19. The variation of Sun's galactocentric radius (upper panel) and vertical displacement from the disk (lower panel) as calculate for different potentials: axisymmetric potential (black); potential including Galactic bar (red); potential including spiral arm (blue); potential including both bar and arm (green). To show different lines in the lower panel better, we plot the variation of the Sun's vertical displacement over a shorter time scale.

Figure 20. The magnitude of the tide-induced flux, f_c, generated by the axisymmetric potential model (upper panel) and the relative flux difference, $\Delta f_c/f_c$, generated by asymmetric Galactic potential models (lower panel) over the past 5 Gyr with a sample of 3×10^4 comets. The potentials are: axisymmetric potential only (black); including the arms (blue); including the Galactic bar (red); including both the arms and the Galactic bar (green).

the non-axisymmetric components do not alter the flux very much. Although the perturbation from the arms can change the solar orbit slightly, the resulting change in the perturbation of the Oort cloud is minimal. The changed tidal force may change some individual cometary orbits, but has little effect on the overall injected comet flux, because the effect of the tide depends also on the distribution of the comets, which is nearly isotropic. We also see that the arms modify the cometary flux more than the bar, consistent with its larger impact on the stellar density. (The limited number of injected comets contributes to the sharp peaks in the relative flux difference, $\Delta f_c/f_c$, after 3 Gyr.)

We also investigated the sensitivity of the solar motion and comet flux to the pattern speed of the asymmetric components. We find that the closer the pattern speed of the arms is to the angular velocity of the Sun, the larger the perturbation from the arms is. (We can understand this in terms of a resonance.) Meanwhile, the perturbation from the bar is not sensitive to the bar's pattern speed.

Finally, we also find that the distribution of b_c and l_c of the comet flux does not change very much for different non-axisymmetric components of the Galactic potential.

In summary, we find that the model predictions of the tide-induced cometary flux are generally insensitive to changes in the non-axisymmetric components of the Galactic potential, except when a resonance between the arms and the solar orbit occurs, which increases the variation in the cometary flux.

8.2   Variations of the prior

As discussed earlier, the evidence depends on the prior distribution adopted for the model parameters. As this prior frequently cannot be determined with any certainty, it is important to investigate the
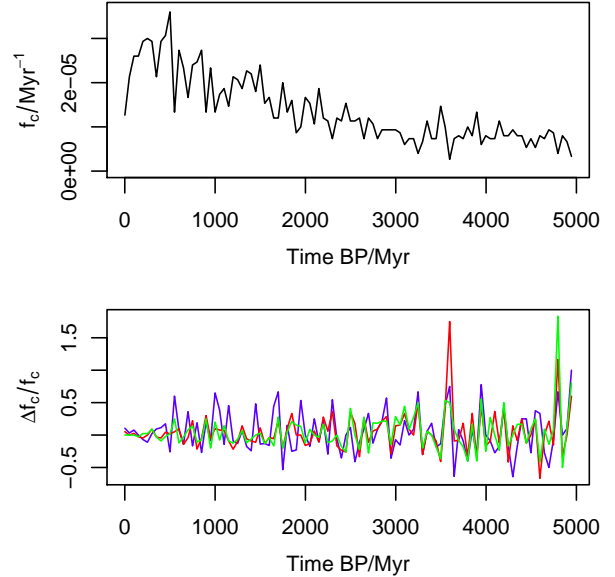
sensitivity of the evidence to changes in the prior.[8] To complete the calculation of evidences for dynamical models, we also vary the other three initial conditions, $V_R(t = 0 \text{ Myr})$, $z(t = 0 \text{ Myr})$, and $V_z(t = 0 \text{ Myr})$, in the EncTideSigProb models, which we previously kept constant. Together with SigProb, EncSigProb and TideSigProb, this was previously the best favoured model (Table 6). We made numerous changes in the priors by altering their parameter ranges, and re-did all necessary Monte Carlo samplings, numerical simulations, and likelihood calculations and recomputed the Bayes factors. Some of our results are shown in Table 7.

The difference in Bayes factors for random models (Rand-Prob, RandBkgProb) and periodic models (SinProb, SinBkgProb) with different prior distributions is less than five. The Bayes factors also remain less than ten so they remain no better explanations of the cratering data than the Uniform model. Thus our former conclusions about these models are not very sensitive to plausible changes in the priors.

The TideSigProb models in which other parameters are varied have nearly the same evidences as the TideSigProb models listed in Table 6, so these too are insensitive to these changes in the priors. We also see that the SigProb model with positive λ has Bayes factors much lower than SigProb with negative λ for both the basic150 and basic250 data sets.

The dynamical models have parameters of the Galaxy potential, Sun's initial conditions and combination ratio parameters (η and ξ) which are listed in Table 5). To keep things simple, we change the fixed parameters and the ranges of the varying parameters individually, and then calculate the evidence by sampling the prior defined by the changed parameter and other parameters shown

---

[8]   A more robust – but also more time-consuming – way of calculating the evidence is presented in **?**.

Table 7. The Bayes factors for various time series models (rows) relative to the uniform model for two different data sets (cf. Table 6). The second column describes what change has been made to the range of which parameter in the prior. The other priors are kept fixed. TideSigProb3–6 refer to the TideSigProb model in which different initial conditions are varied: $V_R(t = 0 \text{ Myr})$; $z(t = 0 \text{ Myr})$; $V_z(t = 0 \text{ Myr})$; all three (respectively)

models	varied prior	Bayes factor for basic150	Bayes factor for basic250
RandProb	none	4.4	3.0
	$\sigma = 2\bar{\sigma}_i$	2.0	4.8
	$\sigma = 1/2\bar{\sigma}_i$	2.2	4.7
	$N = 2N_{\text{ts}}$	1.9	1.8
	$N = 1/2N_{\text{ts}}$	2.4	7.6
RandBkgProb	none	1.8	2.2
	$\sigma = 2\bar{\sigma}_i$	1.6	3.7
	$\sigma = 1/2\bar{\sigma}_i$	1.8	2.6
	$N = 2N_{\text{ts}}$	1.5	1.5
	$N = 1/2N_{\text{ts}}$	2.4	2.9
SinProb	none	0.34	0.43
	$10 < T < 100$	0.12	0.14
	$2\pi/300 < \omega < 2\pi/10$	0.34	0.39
	$10 < T < 300$	0.88	5.4×10^{-2}
SinBkgProb	none	1.0	1.0
	$10 < T < 100$	0.90	0.88
	$2\pi/300 < \omega < 2\pi/10$	1.0	1.0
	$10 < T < 300$	1.8	1.4
SigProb	none	15	2.0×10^2
	$0 < t_0 < 1.2\tau_{\max}$	13	1.4×10^2
	$-100 < \lambda < 100$	7.7	1.0×10^2
	$0 < \lambda < 100$	1.3×10^{-2}	1.8×10^{-3}
SinSigProb	none	6.4	80
	$0 < t_0 < 1.2\tau_{\max}$	8.3	71
	$2\pi/300 < \omega < 2\pi/10$	9.9	97
TideSigProb3	none	9.0	1.7×10^2
TideSigProb4	none	9.1	1.7×10^2
TideSigProb5	none	9.0	1.7×10^2
TideSigProb6	none	11	1.6×10^2

in Table 5. We calculate evidences for dynamical models with double or half the disk mass (M_d), halo mass (M_h), standard deviation of the initial value R (σ_R), and the range of the varying ratio between the EncTideProb (or TideProb) and SigProb models (η). In addition, previous studies suggest that the number of tide-induced LPCs is not identical to the encounter-induced LPCs, i.e. $\xi \neq 1$ (Heisler, Tremaine & Alcock 1987; Rickman et al. 2008). Thus we multiply the ratio between the tide-induced flux and the encounter-induced flux (ξ) by a factor of 4 or 1/4 for the sensitivity test.

The resulting Bayes factors calculated for the basic150 data set are shown in Table 8. In each row we see little variation: the Bayes factors are relatively insensitive to these parameters. This means that either the parameter space of the EncTideSigProb1 model is evenly favoured by the basic150 data set, or the data are unable to discriminate between the compound dynamical models.

The model prediction of the anisotropic LPCs (see Figure 17) depends to a greater or lesser extent on the Galactic potential, the Sun's initial condition, the Oort Cloud model, and the model of encounters. We vary the model parameters in the same way as we did in Table 8 and simulate ten million orbits of DLDW comets perturbed by the tide and ten samples of stellar encounters backwards to 10 Myr ago. We find that the latitude distribution of the LPC per-

ihelia is not sensitive to the change of the Galactic halo mass, the initial conditions of the Sun, or the direction of the solar apex. The amplitudes of the peaks in the latitude distribution are reduced if we decrease the mass of the Galactic disk or increase the stellar masses, which make the stellar encounters play a more important role in injecting comets into the loss cone. However, the overall profile of the peaks is not changed in the latitude distribution.

The peaks in the longitude distribution shift slightly if we change the solar apex direction, the masses of the encounters, or the mass of the Galactic disk. The longitude distribution is not sensitive to changes in the other model parameters.

Finally, we also tested the effect of changing the time step in the (combined) simulations. We simulated four million comets generated from the DLDW model perturbed by the tide and ten samples of stellar encounters backwards to 10 Myr ago using a time step of 0.001 Myr (as opposed to 0.01 Myr). We find little change in either the latitude or longitude distributions. In addition, we see only 4% more comets injected when using this smaller time step.

In summary, we find that the overall shape of the angular distribution of LPC perihelia in both longitude and latitude is not very sensitive to changes in the model parameters, in particular not to

Table 8. The Bayes factors for EncProb1, EncTideProb1 and EncTideProb1 for basic150 with different Galaxy parameters.

models	none	$2M_d$	$1/2M_d$	$2M_h$	$1/2M_h$	$2\sigma_R$	$1/2\sigma_R$	$\xi = 4$	$\xi = 1/4$	$0 < \eta < 8$	$0 < \eta < 2$
EncProb1	1.5	2.5	3.4	2.5	4.1	2.3	2.6	—	—	—	—
EncTideProb1	1.0	2.1	2.3	2.6	3.5	1.8	1.0	1.5	0.73	—	—
EncTideSigProb1	11	15	11	13	12	12	11	12	10	13	8.8

the initial distribution of Oort Cloud comets, not to the masses of Galactic halo and disk, and not to the initial conditions of the Sun.

9 DISCUSSION AND CONCLUSION

We have built dynamical models for the impact rate and angular distribution of comets induced by the Galactic tide and stellar encounters, as modulated by the solar motion around the Galaxy. Without using the approximate methods (the averaged Hamiltonian or impulse approximation), we numerically simulate the tide-induced flux and encounter-induced flux separately. We use these to validate the use of proxies for tide-induced flux, G_3, and for the encounter-induced flux, $\gamma_{\rm bin}$, in our models.

Using the Bayesian evidence framework, we find that the pure trend model (SigProb) together with the dynamical models including a trend component (EncSigProb, TideSigProb and EncTideSigProb) for the cratering record are better favoured than other models we have tested. The trend component indicates a decreasing cratering rate ($\lambda < 0$) towards the past over the past 100 Myr (Shoemaker 1998; Gehrels, Matthews & Schumann 1994; McEwen, Moore & Shoemaker 1997; Bailer-Jones 2011a). This suggests that either the asteroid impact rate or the preservation bias or both dominates the cratering record. Because the craters in our data sets are larger than 5 km, the preservation bias may not be very significant over this time scale. The disruption of a single large asteroid could explain the trend in the data, as suggested by (Bottke, David & David 2007). In addition, our models, which include the solar apex motion, can properly predict the anisotropic perihelia of LPCs without assuming a massive body in the outer Oort Cloud or an anisotropic Oort Cloud.

The EncTideSigProb, EncSigProb and TideSigProb models have Bayes factors of the same magnitude as the SigProb model, which indicates that either the tide and encounter components are unnecessary in modelling the temporal distribution of craters, or the data cannot effectively discriminate between the models.

The stochastic component in the comet flux arising from encounters – as represented by the term γ – in the EncProb and EncTideProb models can slightly increase their evidence relative to the TideProb model. We have performed a sensitivity test by changing the prior PDF over the parameters in the dynamical models and other time series models, and find only small changes of the Bayes factors.

The asymmetrical components in the Galactic potential could, in principle, increase the time-variation of the comet flux and hence impact rate predicted by the dynamical models, by inducing larger deviations of the Sun's motion from a circular orbit and thus larger changes in the local stellar density. It turns out that the non-axisymmetric component has relatively little impact on the predicted cometary flux, with the exception of when the Sun is in co-rotation with the spiral arms. In that case the transient resonance can produce large variations in the flux.

By including the solar apex motion, our dynamical models for anisotropic LPCs can predict reasonably well the distribution of Galactic latitude and longitude in a set of 102 dynamically new comets. In this model, the asymmetry in the distribution of Galactic latitudes caused by the Sun's current location and its motion over the past 10 Myr (comparable with the time scale of a comet shower).

The two narrow peaks in the cometary perihelia at $l_c = 135°$ and $l_c = 315°$ could be caused by a handful of strong stellar encounters encountering the Sun with their encountering velocities in the direction of antapex in the HRF. On the other hand, we might also see something similar due to the periodic orbital motion about the Sun of a massive body (such as a brown dwarf) residing within the Oort cloud (Matese, Whitman & Whitmire 1999; Matese & Whitmire 2011). However, our dynamical model, which takes into account the solar apex motion, can predict the longitudinal asymmetry without assuming the existence of such a body. In addition, the latitude distribution of LPC perihelia predicted by our simulations is consistent with the theoretical prediction, although one peak in the observed distribution is not properly predicted by our simulations. The synergy effect between the encounters and the tide cannot entirely eliminate the anisotropy induced by either the tide or the encounters.

A non-uniform distribution in the perihelion direction of encounters was found by García-Sánchez et al. (2001), although the signal is of questionable significance due to the incompleteness, i.e. faint stars which high velocities being too faint after 10 Myr for Hipparcos to have observed.

An anisotropy in the longitude of LPCs will not correspond to an anisotropy in longitudes of impacts on the Earth's surface due to the rotation of the Earth and its orbit about the Sun. Some latitude variation may be expected, despite the long-term variation in inclination and obliquity of the Earth's orbit (Le Feuvre & Wieczorek 2008; Werner & Medvedev 2010). Disrupted comets generally retain their original orbital plane (Bottke et al. 2002), so the resulting asteroids would tend to impact in the plane perpendicular to solar apex. Yet these are all higher order effects which would be difficult to convincingly detect and relate to the solar orbit in the analysis of terrestrial impact craters.

Our modelling approach has, like any other, introduced various assumptions and approximations. We have ignored the synergy effect between the Galactic tide and stellar encounters highlighted by Rickman et al. (2008). We instead simply sum the tide-induced flux and the encounter-induced flux in the ratio ξ to 1. Because the cometary impact rate modulated by the solar motion around the Galactic center seems to be unnecessary in order to explain the data, the synergy effect, which is also influenced by the solar motion, may not change the result significantly. In addition, we use a decreasing impact rate towards the past (negative trend component) to model the combined effect of preservation bias and asteroid impact rate. In modelling the angular distribution of the LPC perihelia, the sample noise in the comets injected into the observable zone

prevent us from building a more robust model, especially for the longitude distribution. This problem could be resolved by calculating perturbations based on a more accurately measured Galactic tide and using an actual catalogue of encountering stars in the solar neighborhood as opposed to our stochastic model of plausible encounters.

In common with some other studies (e.g. Rickman et al. (2008); Gardner et al. (2011); Fouchard et al. (2011); Wickramasinghe & Napier (2008)), we have ignored the perturbing effect on comets from the giant planets, although we acknowledge that the giants planets could influence the predicted LPC flux in particular (Kaib & Quinn 2009). The planetary perturbations can also change the fraction of the inner Oort cloud comets among the injected LPCs (Kaib & Quinn 2009), which in turn could change the angular distribution of the LPC perihelia. However, these perturbations should not have a significant effect over the relatively short time scale of 10 Myr which we use in the simulations to generate the LPC distribution. As the main goal of our work is to study the variable effect of the solar orbit on the LPC flux and angular distribution, rather than to predict the absolute LPC flux precisely, our conclusions should not be overly affected by neglecting the giant planets in this way.

In the future, the Gaia survey allow us to detect many more recent stellar encounters down to fainter magnitude limits and larger distances than Hipparcos, thereby allowing us to extend the time scale over which we can get a complete sample of recent stellar encounters. The Gaia magnitude limit of G=20 which is low enough to cover the high velocity stars in a time scale of 10 Myr. For example, a star with absolute magnitude of 10 and a velocity of 80 km/s in the HRF would move 800 pc in 10 Myr and so have an apparent magnitude of 19.5. Thus Gaia will be able to observe all stars more massive than early M dwarfs (and thus essentially all relevant stars) encountering the solar system over the past 10 Myr. For more recent timescales Gaia can observe even less massive objects. Moreover, the Gaia catalogue of more massive stellar encounters (stars with absolute magnitudes larger than that of the Sun) may shed light on the study of terrestrial craters over since the beginning of the Phanerozoic era, some 550 Myr ago. Gaia can further improve the measurement of Sun's initial conditions and the potential of the Galaxy (Lindegren et al. 2008; Koposov, Rix & Hogg 2010). After including planetary perturbations, this would make the simulation of cometary orbits accurate enough to trace the stellar encounter back to the time when it generated comet showers and corresponding terrestrial craters (Rickman et al. 2012).

REFERENCES

Alvarez L. W., Alvarez W., Asaro F., Michel H. V., 1980, Science, 208, 1095

Alvarez W., Muller R. A., 1984, Nat., 308, 718

Bailer-Jones C. A. L., 2009, International Journal of Astrobiology, 8, 213

Bailer-Jones C. A. L., 2011a, MNRAS, 416, 1163

Bailer-Jones C. A. L., 2011b, MNRAS, 418, 2111

Bailer-Jones C. A. L., 2012, A&A, 546, A89

Bate R. R., Mueller D. D., White J. E., 1971, Fundamentals of astrodynamics. Courier Dover Publications

Biermann L., Huebner W. F., Lust R., 1983, Proceedings of the National Academy of Science, 80, 5151

Binney J., Tremaine S., 2008, Galactic Dynamics: Second Edition. Princeton University Press

Bogart R. S., Noerdlinger P. D., 1982, AJ, 87, 911

Bottke W. F., David V., David N., 2007, Nature, 449, 48, 10.1038/nature06070

Bottke W. F., Morbidelli A., Jedicke R., Petit J.-M., Levison H. F., Michel P., Metcalfe T. S., 2002, Icarus, 156, 399

Brasser R., Higuchi A., Kaib N., 2010, A&A, 516, A72

Cox D. P., Gómez G. C., 2002, ApJS, 142, 261

Dehnen W., 2000, AJ, 119, 800

Dehnen W., Binney J. J., 1998, MNRAS, 298, 387

Delsemme A. H., 1987, A&A, 187, 913

Dones L., Levison H. F., Duncan M. J., Weissman P. R., 2004a, Icarus, in press

Dones L., Weissman P. R., Levison H. F., Duncan M. J., 2004b, in Astronomical Society of the Pacific Conference Series, Vol. 323, Star Formation in the Interstellar Medium: In Honor of David Hollenbach, Johnstone D., Adams F. C., Lin D. N. C., Neufeeld D. A., Ostriker E. C., eds., p. 371

Drimmel R., 2000, A&A, 358, L13

Duncan M., Quinn T., Tremaine S., 1987, AJ, 94, 1330

Dybczyński P. A., 2002, A&A, 396, 283

Dybczyński P. A., 2005, A&A, 441, 783

Emel'yanenko V. V., Asher D. J., Bailey M. E., 2007, MNRAS, 381, 779

Feng F., Bailer-Jones C. A. L., 2013, ApJ, 768, 152

Fouchard M., 2004, MNRAS, 349, 347

Fouchard M., Froeschlé C., Rickman H., Valsecchi G. B., 2011, Icarus, 214, 334

Francis P. J., 2005, ApJ, 635, 1348

Fujii M., Iwasawa M., Funato Y., Makino J., 2007, PASJ, 59, 1095

García-Sánchez J., Preston R. A., Jones D. L., Weissman P. R., Lestrade J.-F., Latham D. W., Stefanik R. P., 1999, AJ, 117, 1042

García-Sánchez J., Weissman P. R., Preston R. A., Jones D. L., Lestrade J.-F., Latham D. W., Stefanik R. P., Paredes J. M., 2001, A&A, 379, 634

Gardner E., Nurmi P., Flynn C., Mikkola S., 2011, MNRAS, 411, 947

Gehrels T., Matthews M. S., Schumann A. M., eds., 1994, Hazards due to comets and asteroids

Grieve R. A. F., Pesonen L. J., 1996, Earth Moon and Planets, 72, 357

Heisler J., Tremaine S., Alcock C., 1987, Icarus, 70, 269

Hildebrand A. R., Penfield G. T., Kring D. A., Pilkington M., Camargo Z. A., Jacobsen S. B., Boynton W. V., 1991, Geology, 19, 867

Hills J. G., 1981, AJ, 86, 1730

Jetsu L., Pelt J., 2000, A&A, 353, 409

Kaib N. A., Quinn T., 2009, Science, 325, 1234

Kaib N. A., Quinn T., Brasser R., 2011, The Astronomical Journal, 141, 3

Kaib N. A., Roškar R., Quinn T., 2011, Icarus, 215, 491

Kass R. E., Raftery A. E., 1995, Journal of the American Statistical Association, 90, 773795

Khanna M., Sharma S. D., 1983, PASJ, 35, 559

Koposov S. E., Rix H.-W., Hogg D. W., 2010, ApJ, 712, 260

Le Feuvre M., Wieczorek M. A., 2008, Icarus, 197, 291

Levison H. F., Duncan M. J., Brasser R., Kaufmann D. E., 2010, Science, 329, 187

Lindegren L. et al., 2008, in IAU Symposium, Vol. 248, IAU Symposium, Jin W. J., Platais I., Perryman M. A. C., eds., pp. 217–223

Luhman K. L., 2014, The Astrophysical Journal, 781, 4

Majaess D. J., Turner D. G., Lane D. J., 2009, MNRAS, 398, 263

Marsden B. G., Williams G. V., 2008, Catalogue of Cometary Orbits 2008. 17th edition.

Martos M., Yañez M., Hernandez X., Moreno E., Pichardo B., 2004, Journal of Korean Astronomical Society, 37, 199

Matese J. J., Lissauer J. J., 2002, Icarus, 157, 228

Matese J. J., Whitman P. G., Whitmire D. P., 1999, Icarus, 141, 354

Matese J. J., Whitmire D. P., 2011, Icarus, 211, 926

McEwen A. S., Moore J. M., Shoemaker E. M., 1997, J. Geophys. Res., 102, 9231

Melott A. L., Bambach R. K., 2011, Paleobiology, 37, 383

Oort J. H., 1950, Bull Astron Inst Neth Suppl, 11, 91

Pelupessy F. I., Jänes J., Portegies Zwart S., 2012, New A, 17, 711

Pelupessy F. I., van Elteren A., de Vries N., McMillan S. L. W., Drost N., Portegies Zwart S. F., 2013, A&A, 557, A84

Portegies Zwart S., McMillan S. L. W., van Elteren E., Pelupessy I., de Vries N., 2013, Computer Physics Communications, 183, 456

Raup D. M., Sepkoski J. J., 1984, Proceedings of the National Academy of Science, 81, 801

Rickman H., 1976, Bulletin of the Astronomical Institutes of Czechoslovakia, 27, 92

Rickman H., Fouchard M., Froeschlé C., Valsecchi G. B., 2008, Celestial Mechanics and Dynamical Astronomy, 102, 111

Rickman H., Fouchard M., Froeschlé C., Valsecchi G. B., 2012, Planet. Space Sci., 73, 124

Rickman H., Fouchard M., Valsecchi G. B., Froeschlé C., 2005, Earth Moon and Planets, 97, 411

Rohde R. A., Muller R. A., 2005, Nat., 434, 208

Schönrich R., 2012, MNRAS, 427, 274

Schönrich R., Binney J., Dehnen W., 2010, MNRAS, 403, 1829

Shoemaker E. M., 1998, JRASC, 92, 297

Wainscoat R. J., Cohen M., Volk K., Walker H. J., Schwartz D. E., 1992, ApJS, 83, 111

Weissman P. R., 2007, in IAU Symposium, Vol. 236, IAU Symposium, Valsecchi G. B., Vokrouhlický D., Milani A., eds., pp. 441–450

Werner S. C., Medvedev S., 2010, Earth and Planetary Science Letters, 295, 147

Wickramasinghe J. T., Napier W. M., 2008, MNRAS, 387, 153

Wiegert P., Tremaine S., 1999, Icarus, 137, 84

Wisdom J., Holman M., 1991, AJ, 102, 1528

Yabushita S., 1996, MNRAS, 279, 727